THESIS

A REDUCED CHEMICAL KINETIC MECHANISM FOR COMPUTATIONAL FLUID DYNAMICS SIMULATIONS OF HIGH BRAKE MEAN EFFECTIVE PRESSURE, LEAN-BURN NATURAL GAS ENGINES

Submitted by

David Martinez Morett

Department of Mechanical Engineering

In partial fulfillment of the requirements

For the Degree of Master of Science

Colorado State University

Fort Collins, Colorado

Fall 2012

Master's Committee:

Advisor: Anthony J. Marchese

Daniel B. Olsen
David S. Dandy

ABSTRACT

A REDUCED CHEMICAL KINETIC MECHANISM FOR COMPUTATIONAL FLUID DYNAMICS SIMULATIONS OF HIGH BRAKE MEAN EFFECTIVE PRESSURE, LEAN-BURN NATURAL GAS ENGINES

Recent developments in numerical techniques and computational processing power now permit time-dependent, multi-dimensional computational fluid dynamics (CFD) calculations with detailed chemical kinetic mechanisms using commercially available software. Such computations have the potential to be highly effective tools for designing lean-burn, high brake mean effective pressure (BMEP) natural gas engines that achieve high fuel efficiency and low emissions. Specifically, these CFD simulations can provide the analytical tools required to design highly optimized natural gas engine components such as pistons, intake ports, pre-combustion chambers, fuel systems and ignition systems. To accurately model the transient, multi-dimensional chemically reacting flows present in these systems, detailed chemical kinetic mechanisms are needed that accurately reproduce measured combustion data at high pressures and lean conditions, but are of reduced size to enable reasonable computational times. Prior to the present study, these CFD models could not be used as accurate design tools for application in high BMEP lean-burn gas engines because existing reduced chemical kinetic mechanisms failed to accurately reproduce experimental flame speed and ignition delay data for natural gas at high pressure (40 atm and higher) and lean (0.6 equivalence ratio (ϕ) and lower) conditions. Existing methane oxidation mechanisms had typically been validated with experimental conditions at atmospheric and intermediate pressures (1 to 20 atm) and relatively rich stoichiometry. Accordingly, these kinetic mechanisms were not adequate for CFD simulation of natural gas

combustion for which elevated pressures and very lean conditions are typical. This thesis describes an analysis, based on experimental data, of the laminar flame speed computed from numerous, detailed chemical kinetic mechanisms for methane combustion at pressures and equivalence ratios necessary for accurate high BMEP, lean-burn natural gas engine modeling. A reduced mechanism that was shown previously to best match data at moderately lean and high pressure conditions was updated for the conditions of interest by performing sensitivity analysis using CHEMKIN. The reaction rate constants from the most sensitive reactions were appropriately adjusted to obtain better agreement at high pressure lean conditions. An evaluation of two new reduced chemical kinetic mechanisms for methane combustion was performed using Converge CFD software. The results were compared to engine data and a significant improvement on combustion performance prediction was obtained with the new mechanisms.

ACKNOWLEDGMENTS

To my family for their love and support; to my advisor, Professor Anthony Marchese, for his teachings and the prospects he opened to me; to the Prometheus team for this great opportunity and the continuation they provided; and to all my friends here and in my hometown, and especially to my best friend in the world, Kathryn.

This work was sponsored by a grant to Colorado State University from Prometheus Applied Technologies, LLC. The work was also made possible by a software grant from Convergent Science, Inc. that provided an academic license for CONVERGE™ at no charge to the project.

TABLE OF CONTENTS

LIST OF TABLES

LIST OF FIGURES

1. INTRODUCTION

Natural gas is highly important for the U.S. economy and many other economies as an energy source. In 2010, natural gas provided 25% of the total energy consumed in the U.S.A., and the majority of this natural gas was produced domestically [1]. Electricity and power generation accounted for 31% of the end-use consumption from the total natural gas (NG) usage, and the current trend shows an increase in electricity production using natural gas compared to previous years. There are also more natural gas reserves that have been recently identified, increasing the global reserves by 12.3 trillion cubic meters to 208.4 trillion cubic meters [2]. A big share of these recently discovered reserves are obtained from shale gas, which is extracted from dense shale rock formations, and it has propelled the natural gas production from shale to a 25% growth of U.S. gas production in just a decade, and it is estimated to grow to 50% by the year 2035 [3].

Natural gas combustion also produces fewer emissions when compared to other fuels and provides a safe, locally independent, and clean energy source. The U.S. trend is similar to the worldwide perspective, where natural gas accounts for 23% of the global energy consumption [4]. The percentage of energy consumption from natural gas combustion is also expected to increase to 44% by 2035. The current perspective for natural gas as an energy source is that it can provide a reliable and inexpensive fuel. There has been significant investment in natural gas projects in countries like the U.S.A. and Mexico where new gas infrastructure projects were recently created with a cost of approximately $10.5 billion USD in order to elevate its consumption by 40% [5].

Natural gas is a naturally occurring hydrocarbon gas mixture, and can be found in nature as a composition of mostly methane with slightly larger hydrocarbons (mainly *n*-alkanes); and

other species such as carbon dioxide, nitrogen, and hydrogen sulfide. This gaseous fuel is typically obtained from natural occurring processes, and can be found in deep underground rock formations close to other hydrocarbon reservoirs like coal beds and petroleum. Other energy sources similar to natural gas are landfill gas or biogas which are produced from the biodegradation of organic waste from cities or industrial processes; synthetically produced gas (syngas); and as by-product of other processes, for example wood gasification. The chemical composition of natural gas and these other gaseous fuels depends on its production origin. Well-head gas for example, which is obtained directly from oil deposits, is rich in methane (~90% Vol.), and the rest being larger alkanes such as ethane, propane, butane, up to heptane and others in small traces. On the other hand, landfill gas can be composed of 50% methane and 50% carbon dioxide by volume. This diversity in gaseous fuel composition affects the technology used to convert the chemical energy to mechanical energy, creating research and market opportunities; and it continually increases the fuel resources thought to be in existence.

The energy contained in natural gas is released through the oxidation process, or combustion, and transformed into thermal energy. This thermal energy is then used to produce work or mechanical energy by burning in internal combustion engines or gas turbines or fuel cells; work that can then be used to produce electricity. Natural gas is also used for domestic appliances to heat stoves or furnaces, and it is also used as a fuel in the transportation sector. Examples of technologies used for power generation using natural gas include internal combustion engines, and turbine engines.

Current industry trends demand higher engine thermal efficiency while meeting increasingly strict environmental regulations for pollutant emissions. One option to achieve these objectives in natural gas (NG) engines is to combine high brake mean effective pressure (BMEP)

with lean-burn natural gas combustion. Computational fluid dynamics (CFD) simulations can provide the analytical tools required to design highly optimized natural gas engine components such as pistons, intake ports, pre-combustion chambers, fuel systems and ignition systems. If coupled with accurate chemical kinetic mechanisms, CFD models can produce predictive combustion simulation results. The accuracy of the predictions from the CFD simulations largely depends on various computational sub-models and the proper specification of the boundary conditions. These effects were studied in a previous work [6].

With the advances in computational techniques, and with the increasing demand for natural gas engines to supply the global energy consumption, the need for an accurate chemical kinetic mechanism for CFD modeling of methane combustion at high pressures and lean conditions is necessary. The need for a reduced mechanism arises from the fact that the number of chemical species in a kinetic mechanism is proportional to the number of equations in the chemical source vector, and elimination of species speeds up the computation due to reduction in number of variables in the system of partial differential equations. For this reasons, reduced detailed chemical kinetic mechanism is required for the engine design industry were long computational times are prohibitive. The ultimate achievement of this reduced mechanism is to provide with a more reliable model for the CFD simulation that contributes to the development of better engine components.

Prior to the present study, CFD models had marginal predictability especially for application in high BMEP lean-burn gas engines because existing detailed (approx. 100 species) and reduced (approximately 20 species) mechanisms fail to accurately reproduce experimental flame speed and ignition delay data for natural gas at high pressure (higher than 40 atm) and lean (lower than 0.6 equivalence ratio (ϕ)) conditions. Due to the high computational time used by

CFD codes, reduced kinetic mechanisms are the only viable option to execute simulations with reasonable computation times. Approximately 24 hours for a combustion cycle simulation would be considered reasonable in the engine design industry using a personal computer (PC) or a cluster of PC's, with up to date software and hardware.

1.1 Mechanism Validation: Laminar Flame Speed and Ignition Delay

Existing methane oxidation mechanisms have typically been validated with experimental conditions at atmospheric and intermediate pressures (1 to 20 atm) and relatively rich stoichiometry ($\phi > 0.8$). The need for validated chemical kinetic mechanisms that are accurate at high pressures for application in internal combustion engines has been well recognized [7,8]. However, there are only limited high pressure experimental data (e.g., flame speed measurements) available to validate these mechanisms. In a previous study [6], the best available reduced combustion mechanism used in CFD simulations for methane combustion was found to be the DRM22 mechanism [9], which is a 22 species kinetic model that was reduced from GRI-Mech1.2 [10]. In the prior work [6], adjustments in the spark model, surface temperatures and turbulence model had to be made to compensate for the over-prediction of the fuel burning rate from DRM22. This technique represented a deviation from the realistic physical parameters found in an internal combustion engine.

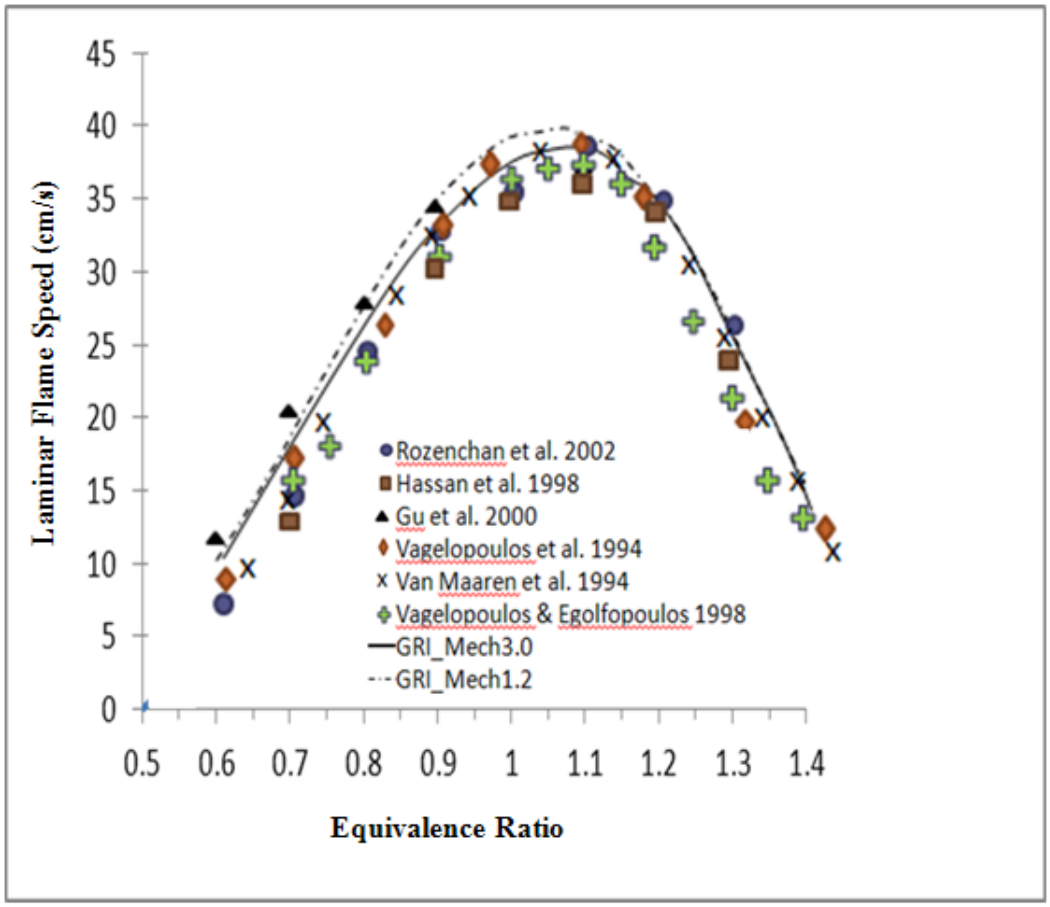

Figure 1. Comparison between experimental and predicted laminar flame speed for methane/air at 1 atm as a function of equivalence ratio. Data obtained from reference 7.

Figure 1 compares different experimental and predicted laminar flame speed data for methane/air at 1 atm from different experimental studies (symbols) compared to the predicted laminar flame speed by the GRI-Mech1.2 and GRI-Mech3.0 chemical kinetic models. There is overall agreement between the different experimental measurements, and with the exception of the experimental data from Gu et al. [11]; it can be seen that as the air/fuel ratio goes leaner (equivalence ratio<1 indicates the mixture is fuel lean), there is an over-prediction (~33% flame speed difference at equivalence ratio 0.6) in flame speed computed by the GRI-Mech1.2 and GRI-Mech3.0 mechanisms compared to experimental data.

The effect of pressure on the combustion of methane continues to be an important

research area, since most practical combustion systems operate at pressures of 10 atm or greater. The majority of research in this area has been motivated by industrial gas turbine applications where the operating pressures are in the order of 10 atm. However, there is a critical need in the internal combustion engine industry for providing chemical kinetic mechanisms of reference fuels such as methane, ethane, and propane at high BMEP engine-relevant conditions where combustion pressures are in the order of 60 atm.

Many existing [7,12,13] methane chemical kinetic mechanisms exhibit reasonable performance at pressures less than 40 atm and equivalence ratios greater than 0.7, but these conditions are not representative of lean-burn, natural gas engine operation. Rozenchan, et al.[7] presented experimental laminar burning velocities for methane at pressures up to 60 atm, along with calculated results using GRI-Mech3.0 and GRI-Mech1.2. The calculated results exhibited satisfactory agreement with the data at pressures less than 20 atm, but poor agreement at pressures above 40 atm. It is clear from these studies that many existing methane combustion mechanisms are inadequate for combustion simulations at higher pressures and leaner conditions, which creates a challenge for the design of combustion systems for lean-burn natural gas engines. Compounding this problem is the lack of experimental data at high pressures and lean conditions that can be used to validate kinetic mechanisms.

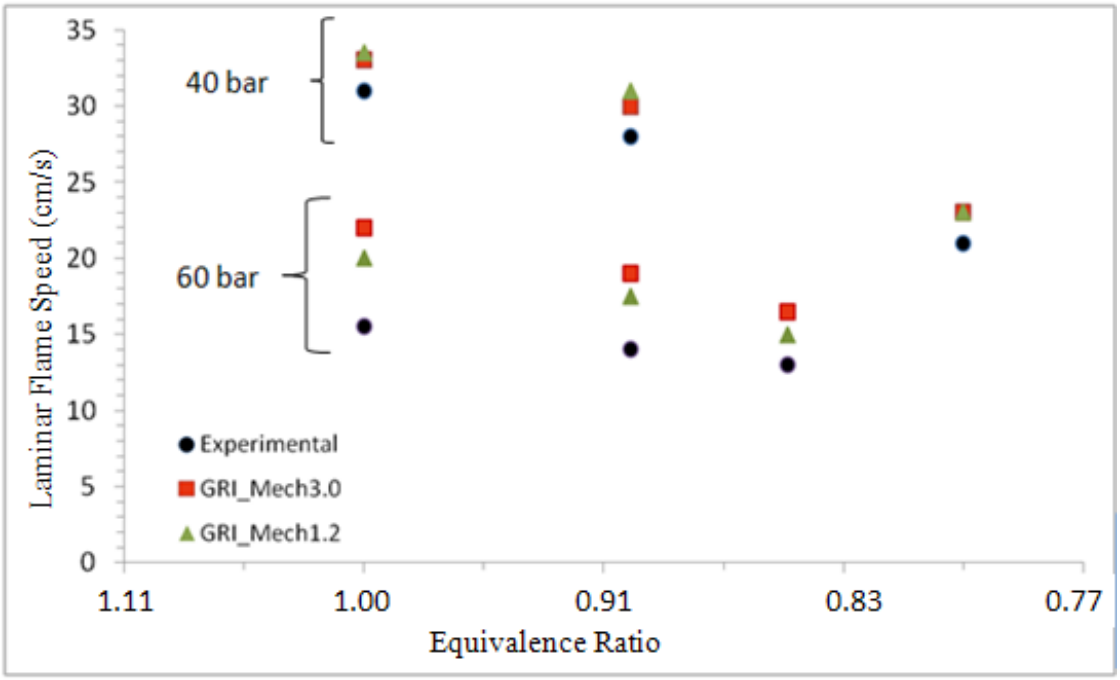

Figure 2. Experimental laminar flame speed as a function of equivalence ratio for CH_4/O_2/He mixtures at 40 and 60 atm compared to predicted computation from the kinetic mechanisms GRI_Mech1.2 and 3.0. Data from reference 7.

Figure 2 is a plot of the experimental laminar flame speed for methane at high pressures (40 and 60 atm) compared to the flame speed predicted by the GRI-Mech1.2 and 3.0 chemical kinetic mechanisms. The diluent used in the experiments consisted of Helium instead of Nitrogen (or air) because of flame instabilities at high pressures that compromise the accuracy of the measurements. As Figure 2 shows, the kinetic mechanisms over predict the flame speed at high pressures, and this error increases with pressure for both the lean and stoichiometric conditions.

The research in natural gas chemical kinetics had a major advance after the most widely used natural gas mechanism, GRI-Mech3.0, was obtained from an extensive research program sponsored by the Gas Research Institute (GRI) during the 1990`s [14]. This sustained research program resulted in successive releases of natural gas kinetic mechanisms including GRI-Mech1.1, 1.2, 2.11, and 3.0, which was the last version released. GRI-Mech3.0 was developed to model the combustion chemistry of methane and other natural gas components (up to 3 carbon

atoms, C_3) at temperatures between 1000 and 2500 K, pressures of 0.01 atm to 10 atm, and equivalence ratios from 0.1 to 5. GRI-Mech3.0 was developed by including all chemical reactions thought to be important for natural gas combustion (ignition and flame propagation) including NO_x chemistry, with the most up-to-date reaction rate constants available at that time. These reaction rate constants were determined by elementary reaction theory and by experimental measurements.

The mechanism GRI-Mech1.2 was reduced by Kazakov and Frenklach [9] using a detailed reduction method that resulted in two reduced mechanisms: DRM22 and DRM19, which contained 22 and 19 species, respectively. The performance of these reduced mechanisms was tested by the authors using ignition delay and laminar flame speed simulations. The accuracy in the prediction of ignition delay by DRM19, compared to GRI-Mech1.2, drops at low temperatures (<1500 K) and higher pressures (up to 10 atm), obtaining a maximum relative error of 37%. The ignition delay computed by DRM22 remained within 4% relative error compared to GRI-Mech1.2. The laminar flame speed predicted by DRM19 was similar to DRM22 at 1 atm. However, at 20 atm of pressure, the performance of DRM19 is more accurate than DRM22, for the lean to stoichiometric conditions.

Several investigators have recently begun to address the limitations of natural gas mechanisms such as GRI-Mech3.0 at high pressures. For example, Petersen, et al. [15] have developed a natural gas chemical reaction mechanism for the oxidation of species containing up to 3 carbon atoms (C_3). In that work, an experimental and modeling study of methane/propane oxidation at high pressures resulted in a mechanism to simulate the experimental results which included shock-tube experiments of methane-propane blends at pressures ranging from 5.3 to 31.4 atm and equivalence ratios from 0.5 to 3.0. The kinetic mechanism of that work was tested

against ignition delay times obtained from the experiments. A continuation of this work resulted in the NUIG NGM version III [16]. The NUIG NGM_ III mechanism consists of 229 species and 1359 reactions. This mechanism calculates ignition delays of natural gas mixtures that are in good agreement with experimental measurements over wide ranges of pressures (up to 45 atm), lean conditions (equivalence ratio of 0.5 and lower) and temperatures (740 – 1550 K) [17,18,19,20,21].

More recently, a reduced kinetic mechanism by Zsély and co-workers [22] was obtained by starting with the NUIG NGM_III mechanism and performing a mechanism reduction strategy using a recently developed simulation error minimization method (SEM). The smallest reduced mechanism published by Zsély and coworkers consisted of 48 species and 186 reactions. This mechanism was shown to accurately reproduce ignition delays with good agreement (less than 3.1% difference) with the full detailed mechanism. The reduced mechanism also compares well to flame speed data at high pressure and lean conditions. However, it is still too large to perform CFD simulations for lean-burn, high BMEP natural gas engines with computation times that are short enough for use in design simulations. The computation time of a reduced mechanism scales linearly with the number of reactions eliminated, and it scales to the square of the number of species in the mechanism [22] and the typical benchmark for a reasonable computational time in the engine design industry is in the order of 1 to 2 days for a full power stroke (combustion cycle).

Several other mechanisms have been developed in recent years that have shown better agreement against a wider experimental data set than GRI-Mech3.0. For example, the high-temperature chemical kinetic mechanism of $H_2/CO/C_1$-C_4 developed by the University of Southern California (also known as USC-Mech II) [23] was formulated as an update to GRI-

Mech3.0 by considering an optimized reaction model of H_2/CO combustion, a comprehensive reaction model of ethylene and acetylene combustion, a reaction mechanism for C_3, and 1,3-Butadiene oxidation at high temperatures. This mechanism was validated for ignition delays, species profiles, laminar flame speeds, flow reactor, and burner stabilized flames. The laminar flame speed validation test for methane was at 1 atm and 300 K.

A mechanism developed by Konnov [24] includes C_1-C_3 hydrocarbon species and detailed N-H-O chemistry for the prediction of NO_x formation. The Konnov mechanism was based on methane combustion and was extended to cover methanol, acetaldehyde, ethanol, and ethylene oxide. The current version (Konnov 0.5) consists of 1200 reactions and 125 species. The mechanism was validated with shock tube experiments, laminar flame speeds (up to 10 atm at near stoichiometric equivalence ratio), and flow reactors.

Another detailed chemical-kinetic mechanism for small hydrocarbon combustion was developed by the combustion research group at the University of California at San Diego (UCSD) [25]. The mechanism was developed with attention to pressures below 100 atm, temperatures above 1000 K, and equivalence ratios up to 3 for premixed systems. This mechanism was built starting with well validated sub-mechanisms for hydrogen, CO and C_1-C_2 combustion. Later, the mechanism was expanded to include methanol, ethane, ethylene, acetylene, propane, propene, propyne and allene.

In a study by Lowry and co-workers [13], a previously developed natural gas mechanism was updated (resulting in "C_4 mechanism") and validated for laminar flame speed at different experimental conditions. The main improvement to the mechanism consisted in changes to the ethyl and vinyl radical decompositions, causing improvements in the prediction of ethane flame speeds at high pressures. This "C_4 mechanism" is a sub-mechanism on butane isomers whose

initial version is contained in the NUIG NGM_ III mechanism [16].

Egolfopoulos and co-workers [26] developed a detailed reaction model for the combustion of n-alkanes up to C_{16}. The resulting "JetSurF" mechanism's goal was to accurately model the combustion of petroleum-derived and non-petroleum derived jet fuels. Validation measurements included ignition delays and species history in shock tubes and flow reactors, as well as propagation speeds and ignition/extinction limits of laminar flame speeds.

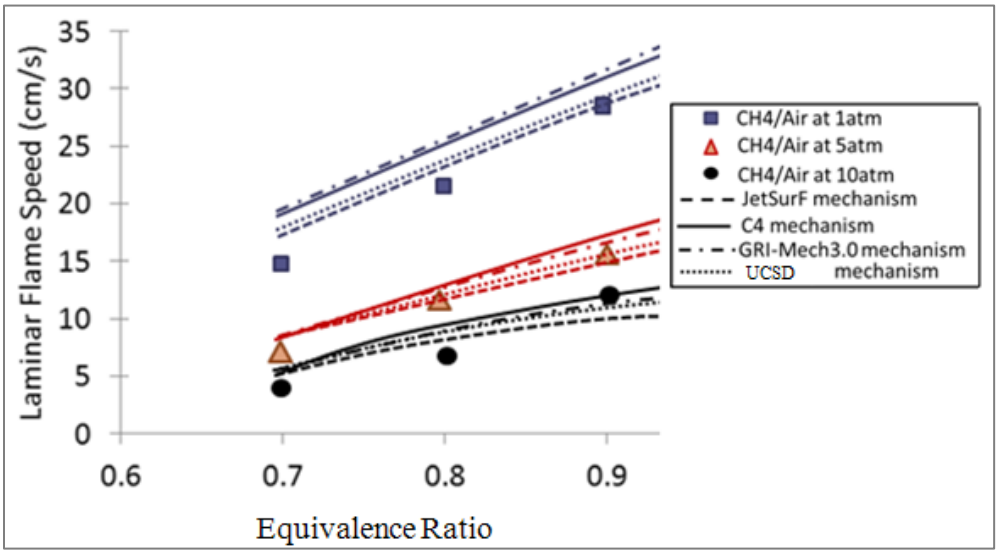

Figure 3. Experimental and kinetic model predictions for laminar flame speed of methane/air at different pressures and equivalence ratios. This figure is from reference 13, not from the modeling of this study.

Figure 3 shows the results of experimental laminar flame speed measurements at 1, 5, and 10 atm and different equivalence ratios compared to predictions using various chemical kinetic mechanisms. All of the kinetic models presented tend to over predict the laminar flame speed as the equivalence ratio approaches the leanest point equivalence ratio (ϕ)=0.7.

The effects of dimethyl ether (DME) addition on the high temperature ignition and burning properties of methane-air mixtures were investigated experimentally and numerically by Chen and co-workers [27]. The ignition enhancement of DME was found to exceed that of hydrogen addition at equivalent amounts. Laminar flame speeds and Markstein lengths were

experimentally measured for methane-air flames with DME addition at atmospheric pressure. The most recent DME mechanism presented in the study was able to reproduce flame speeds of both DME-air and methane-air flames. The uni-molecular decomposition of DME was theoretically studied together with experimental data at pressures up to 10 atm [28]. The model showed improved agreement compared to oxidation data modeled in prior work (Chen et al. 27). The revised mechanism showed good agreement against high and low temperature flow reactor and jet-stirred reactor data, shock tube ignition delays, and laminar flame speeds measurements.

A high pressure (up to 100 bar) detailed chemical-kinetic model for homogeneous combustion of C_1 and C_2 in the intermediate temperature range (500-1100 K) has been developed and validated experimentally by Rasmussen and coworkers [29]. The resulting mechanism was extended with a number of reactions, critical at high temperature, and tested against data from shock tubes, laminar flames and flow reactors.

Huang and Bushe measured the ignition delay of methane-air mixtures enriched with small fractions of ethane/propane at temperatures from 900 to 1400 K, and pressures from 16 to 40 atm [30]. The addition of ethane/propane was found to promote ignition at temperatures below 1100 K. A detailed kinetic mechanism was used to investigate the interaction between ethane/propane and the ignition chemistry of methane at the conditions mentioned.

The use of laminar flame speed and ignition delay data as global test parameters is standard practice in the development of comprehensive oxidation mechanisms for hydrocarbons [31]. Accordingly, laminar flame speed calculations were used in this study as a means to test the performance of the different mechanisms. The laminar flame speed was chosen because it provides a global flame response by accounting for thermal and transport effects. Additionally, some experimental data exist to compare the predictions of kinetic mechanisms. Moreover, the

laminar flame speed is an important parameter for the CFD simulations of internal combustion engines since it largely defines the speed at which combustion waves propagate in premixed engines, ultimately affecting the in-cylinder pressure history.

Unfortunately, there is a lack of experimental laminar flame speed data for natural gas species at the elevated pressures of lean-burn engines that can be used to validate current detailed and reduced chemical kinetic mechanisms. Studies providing such experimental data are scarce [7,31] and the maximum pressures that are reported in these references are less than 60 atm at an equivalence ratio of 0.85. The typical operation for lean-burn natural gas engines can be up to 80 atm at the time of ignition with equivalence ratios as low as 0.55.

In the present study, two new reduced chemical kinetic mechanism are presented, (the "MD19" and the "Nagy21-Burke-MD19" mechanisms) that are sufficiently compact (~20 species and less than 100 reactions) and accurate at high pressures to enable detailed chemistry CFD simulations of lean-burn, high BMEP gas engines. An emphasis on H_2/O_2 chemistry is given in the present study since the H_2/O_2 reaction system is fundamental in the combustion behavior of a variety of fuels. The H_2/O_2 mechanism forms an essential subset of reactions whose rate constants are among the most sensitive for combustion simulation of all hydrocarbons [32,33]. Using this H_2/O_2 sub-mechanism it is expected to affect the reactivity of the proposed reduced mechanisms by using hydrogen as a reactant in the fuel. The Methane Number designation can be used to surrogate the higher alkane content in natural gas. The Methane Number can be defined as the percentage by volume of methane blended with hydrogen that exactly matches the knock intensity of an unknown gas mixture under specified operating conditions in a knock testing engine [34].

In this study the MD19 and the Nagy21-Burke-MD19 reduced chemical-kinetic

mechanisms for natural gas combustion were examined by means of CFD simulations at high-pressure and lean conditions. The CFD results are compared against identical simulations using the DRM22 mechanism. The results of the simulations were then compared against measured in-cylinder pressure data. The results show that the computations are highly dependent on the choice of chemical kinetic mechanism and the MD19 and Nagy21-Burke-MD19 reduced mechanism compare much more favorably against measured in-cylinder pressure data.

2. COMPUTATIONAL TECHNIQUES

The numerical techniques used in this work were executed by the PREMIX model from CHEMKIN used to compute steady, laminar, 1-D premixed flames; and the CONVERGE CFD software for computational fluid dynamics simulations.

The PREMIX model solves for the laminar flame speed, at given thermodynamic conditions, using chemical kinetic mechanisms that are on the order of 120 species and 1200 reactions in a reasonable computational time (less than 1 hr). Computations for thermal ignition delay, or autoignition, were performed in the 0-D homogeneous constant volume model from CHEMKIN which solves chemical kinetic mechanisms in the order of 230 species and 1360 reactions. The complexity of CFD computations limits the use to reduced chemical kinetic mechanisms in the size order of 20 species and 80 reactions. The CONVERGE CFD software used in this study solves the detailed chemistry from chemical kinetic mechanisms in CHEMKIN format. The SAGE model incorporated in the CFD software solves the mass and energy equations using detailed chemistry mechanisms.

2.1 PREMIX Laminar Flame Speed

Laminar flame speed calculations were performed using the CHEMKIN PREMIX program. PREMIX computes species and temperature profiles along with the laminar flame speed for one-dimensional, steady, freely propagating premixed laminar flames.

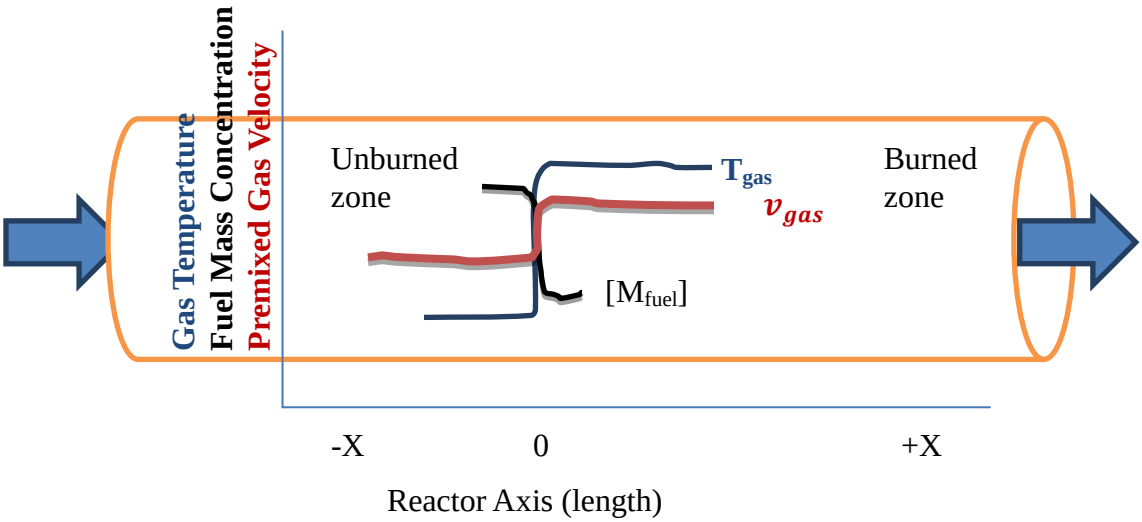

Figure 4. Representation of tubular reactor for flame speed computational model. The coordinate system is fixed to the flame front.

The computation of flame zone within the plug flow reactor provides the solution for the species and temperature profiles in a continuously flowing air/fuel mixture. As described in Figure 4, the solution for laminar flame speed correspond to the velocity at which the total unburned mass flow enters the reactor and provides the fuel/oxidizer to the flame front located at a point of reference (x = 0 in this case). The final solution for laminar flame speed is obtained when there is zero gradient in temperature and species at the flame front as shown in Figure 4.

To formally define the premixed laminar flame speed it is required to discuss a complex physical and mathematical analysis. Since the premixed flame structure can be separated into a preheat zone in which convection and diffusion of species dominate over chemical reactions, and into a reaction zone were chemical reactions and species diffusion balance. Since the mass and

energy are conserved across the flame, from continuity we have:

$$m_{flux} = \rho v = \rho_u v_u = \rho_b v_b \qquad (1)$$

were m_{flux} is the constant mass flux, or laminar burning flux; ρ is the gas density, v the gas velocity, and the subscripts u and b denote the unburned and burned regions respectively. After performing a complex analysis, it can be shown that the laminar flame speed can be approximated as:

$$S_L \approx \sqrt{\alpha RR} \qquad (2)$$

were α is the thermal diffusivity, and RR the overall reaction rate.

The ability to predict the speed at which flames propagate in combustion systems such as internal combustion engines provides an important tool for CFD simulations in which the model best fitting to the experimental results will improve the performance of engines and of combustion systems. Not only is the flame speed an important parameter for simulations, but also for the study of different fuel mixtures and the effect of experimental operation on the formation of pollutants and the performance in engines. Studies in chemical kinetics often refer to flame speed to characterize the reaction mechanisms.

The governing equations for the computation of freely propagating laminar premixed flames by CHEMKIN [35] are discussed in the following section. The specified air/fuel mixture, initial pressure and temperature are provided to the program. One of the main parameters that govern the flame speed computation is the temperature distribution across the domain. The computation of laminar flame speed solves for the transport of heat and chemical species across the flame width, with the use of thermodynamic properties data files together with transport properties and chemical kinetics mechanisms. For the 1-D premixed flame at quasi-steady state model at uniform inlet conditions, CHEMKIN computes the governing conservation equations of:

Continuity

$$\dot{M} = \rho u A \tag{3}$$

Energy

$$\dot{M}\frac{dT}{dx} - \frac{1}{C_p}\frac{d}{dx}\left(\lambda A \frac{dT}{dx}\right) + \frac{A}{C_p}\sum_{k=1}^{K}\rho Y_k V_k C_{pk}\frac{dT}{dx} + \frac{A}{C_p}\sum_{k=1}^{K}\dot{w}_k\, h_k W_k + \frac{A}{C_p}\dot{Q}_{rad} = 0 \tag{4}$$

Species

$$\dot{M}\frac{dY_k}{dx} + \frac{d}{dx}(\rho A Y_k V_k) - A\dot{w}_k W_k = 0 \quad (k = 1,\ldots,K_g) \tag{5}$$

Equation of State

$$\rho = \frac{P\bar{W}}{RT} \tag{6}$$

where x represents the spatial coordinate; $\dot{M}$ is the mass flow rate; T the temperature; Y_k the mass fraction of the kth species; P the pressure; u the velocity of the fluid mixture; ρ the mass density; W_k the molecular weight of the kth species; $\bar{W}$the mean molecular weight of the mixture; R the universal gas constant; λ the thermal conductivity of the mixture; C_p the constant pressure heat capacity of the mixture; C_{pk} the constant pressure heat capacity of the kth species; $\dot{w}_k$the molar rate of production by chemical reaction of the kth species per unit volume; h_k the specific enthalpy of the kth species; V_k the diffusion velocity of the kth species; $\dot{Q}_{rad}$ the heat loss due to gas and particle radiation; and A the cross-sectional area of the stream tube encompassing the flame normalized by the burner area.

The PREMIX model accounts for finite-rate chemical kinetics and multi-component molecular transport. Initial estimates of the temperature profile and intermediate species concentrations are required to solve the problem. The final calculated laminar flame speed

depends on the number of grid points used for the computation of the domain unless a suitably large number of grid points are used.

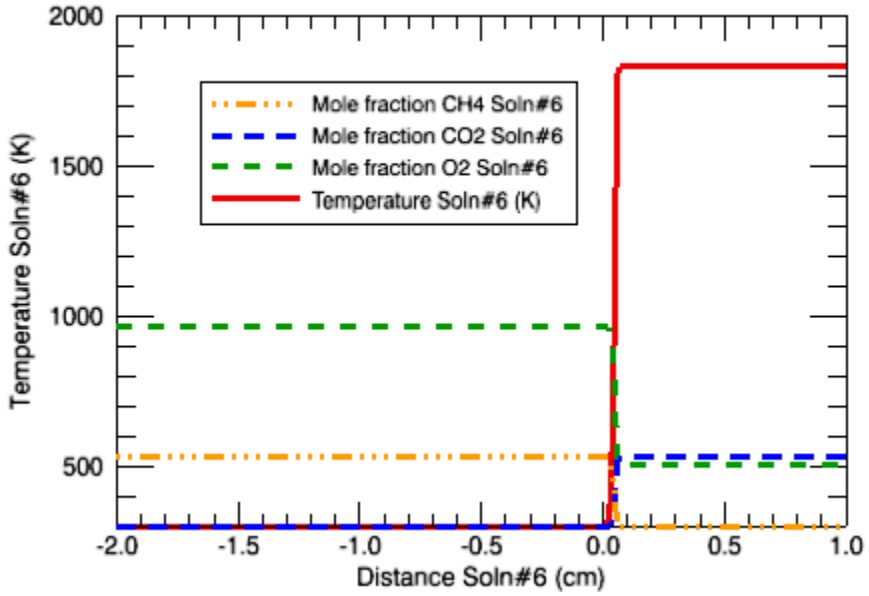

Figure 5. Temperature solution profiles for CH_4/Air at 20 atm and phi=0.7 using the Zsely_50s_251r mechanism [22]. The mole fractions of reactants and product are plotted against the domain distance. Figure obtained from CHEMKIN.

The resulting temperature and species concentration history from the laminar flame speed computation of a selected mechanism is presented in Figure 5. The laminar flame speed obtained from a distribution as in Figure 5 indicates that the thermal and species gradient across the flame structure is minimal.

To obtain the desired resolution, a series of continuation calculations were done by increasing the number of grid points until the final result no longer depended on that parameter. It should be noted that the initial estimate of temperature and intermediate species profiles are important to ensure convergence of the initial calculation. However, since each successive continuation calculation uses the results from the previous calculation for the initial species and temperature profile, the final converged solution is not affected by the initial estimate. As shown

in Figure 6, the calculated laminar flame speed converges toward a solution that is independent of the total number of grid points.

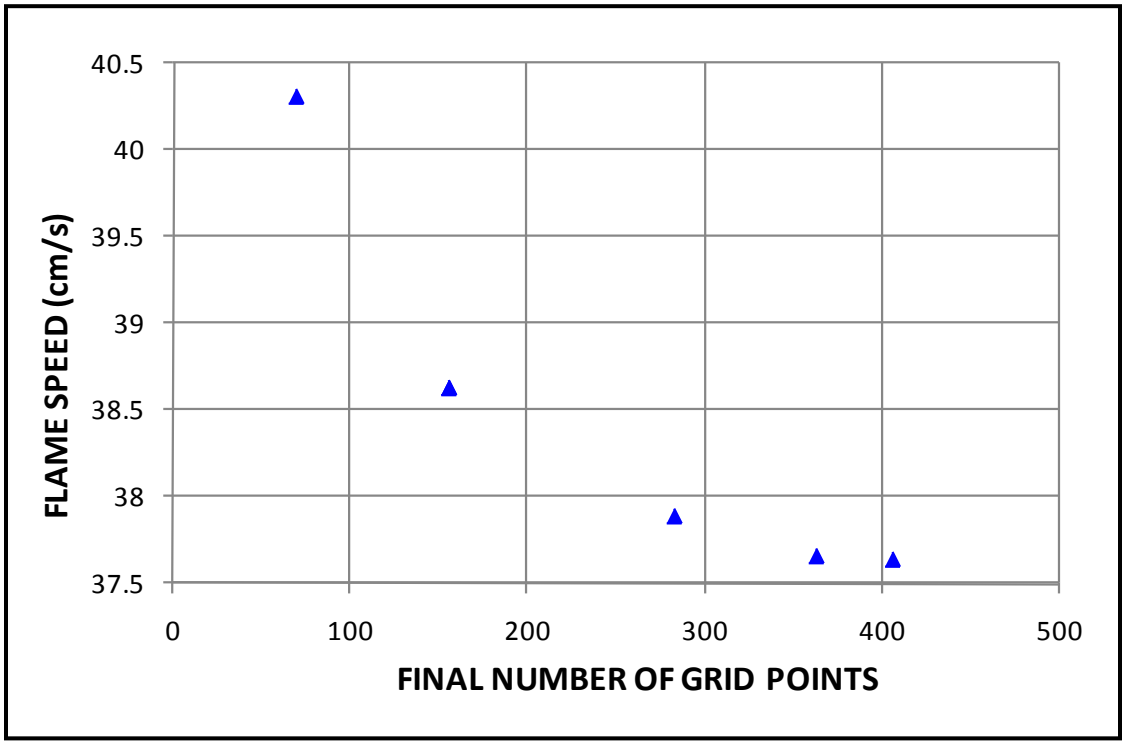

Figure 6. Effect of number of grid points on calculated laminar flame speed from CHEMKIN PREMIX for stoichiometric methane/air at 1 atm as predicted by GRI-Mech3.0.

Laminar flame speed computations were performed at the same conditions as the limited set of available experimental data for high pressure, lean conditions. These experimental data were selected after an extensive literature review of laminar flame speed measurements at high pressures and lean conditions. Ultimately, the data represent the higher pressures and lean conditions found using air for the oxidizer. Some additional data is available at higher pressures but with other inert gases like He and different oxygen compositions. The highest pressures at which lean conditions were found for laminar flame speed measurements using air as oxidizer are presented in Table 1.

Table 1. Experimental laminar flame speed data for lean methane/air mixtures at elevated pressures.

Reference	Pressure (atm)	Equivalence Ratio	Experimental Laminar Flame Speed (cm/s)
Rozenchan et al. [7]	5	0.6	2
Curran et al. [12]	5	0.6	2.5
Lowry et al. [13]	5	0.7	7
Rozenchan et al. [7]	5	0.7	6
Rozenchan et al. [7]	10	0.7	4
Lowry et al. [13]	10	0.7	4
Rozenchan et al. [7]	20	0.7	2

2.1.1 Convergence Techniques for Premix Flame Speed

In order to obtain a solution from the flame speed calculation in CHEMKIN, an appropriate initial condition is required as an input. The different parameters required for the calculation of flame speed are presented in Table 2.

Table 2. Input parameters for the adiabatic laminar flame speed computation in PREMIX model.

Parameter	**Attribute**
Chemical kinetic mechanism file	Elementary reactions set
Thermodynamic data file	Provides the thermodynamic properties of species in the mechanism
Transport data file	Provides with the transport properties of the species
Unburnt Gas Temperature (K)	Specifies the temperature of the Unburnt gas in the model
User-specified estimated temperature	Lists an initial estimate of data points for temperature profile in the reactor model
Optional user-defined temperature constraint	Constraints the flame position to this temperature in the frame of reference
Pressure	Assigns the constant pressure in the model
Grid properties	Assigns initial grid properties for solution of reactor model
Intermediate species-specific properties	Provides with an initial estimate on intermediate species and products concentrations throughout the reactor
Stream property data	Provides an initial estimate of the total mass flow rate inlet for the reactor (initial guess of laminar flame speed)
Inlet species-specific properties	Provides with the air/fuel reactant fractions for the inlet conditions
Solver	Assigns the basic tolerance parameters, and advanced controls for the solution
Continuations	Automates the process of refining the grid and axial position of the reactor model in order to converge with a final solution

The most important settings concern to the initial guess on the flame temperature profile across the reference coordinate, as well as the intermediate species profile, initial air/fuel mass flow rate and the temperature constraint.

Figure 7 shows an example for the flame temperature profile initial estimate.

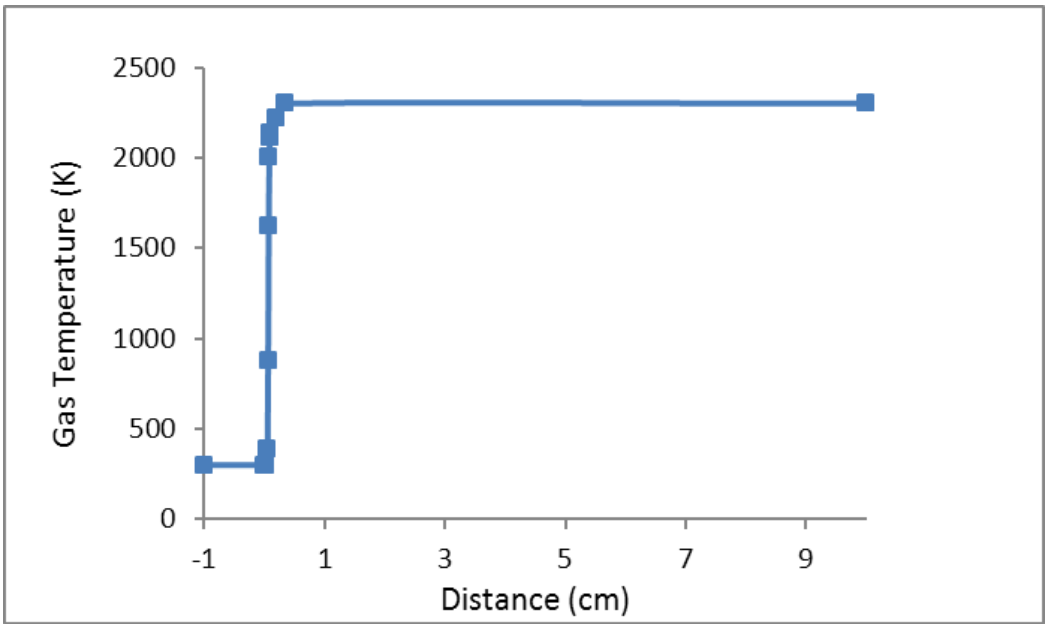

Figure 7. Example of flame temperature profile for the input of the PREMIX solver.

In order to provide with initial estimates of temperature profile, and species concentration across the flame for the computation of laminar flame speed, an initial 0-D constant volume model was used to model the adiabatic flame temperature and intermediate and product species concentrations to be used.

2.2 Computational Fluid Dynamics

The CONVERGE^{TM} CFD software by Convergent Science, Inc. [36] was used in this study. This software facilitates chemically reacting flow modeling with detailed chemistry by incorporating the SAGE [37] solver which allows the user to introduce chemical kinetic mechanisms with a set of CHEMKIN format input files. The SAGE solver has the ability to handle multi-step chemical kinetic mechanisms with forward rate coefficients expressed in the Arrhenius form, and reverse rate coefficients which can either be specified or calculated from the equilibrium constants. SAGE also allows for third-body reactions with the capability of specifying different third body efficiencies for different species [38]. SAGE also allows for the solution of pressure dependent reactions in the Lindemann, Troe, or SRI forms.

The CONVERGE software solves the governing equations for mass and energy conservation at each computational time step, providing intermediate species history throughout the simulation. Besides the ability of solving detailed chemistry, CONVERGE CFD incorporates turbulence models by solving the Reynolds-Averaged Navier-Stokes (RANS) equations and includes an Adaptive Mesh Refinement (AMR) algorithm that creates fine mesh in high gradient regions. The AMR tool increases resolution only at locations of high velocity, temperature, and species gradients, such as the ignition region and the moving flame front.

3. CHEMICAL KINETIC MECHANISM DEVELOPMENT

An extensive literature review was performed to identify relevant kinetic mechanisms for natural gas and other hydrocarbon mechanisms that include methane chemistry. A list of detailed and reduced chemical kinetic mechanisms (up to C_4 fuel species) was compiled from the literature, and is presented in Table 3. The selected mechanisms found in the literature were evaluated in terms of their laminar flame speed predictions and compared against the limited set of experimental data that exist for high pressure lean conditions.

Table 3. List of chemical-kinetic mechanisms evaluated in this study.

Mechanism Name	**Number of Species and Elementary Reactions**	**Reference**
GRI-Mech3.0	51 species and 325 reactions	Smith et al. [10]
DRM22	22 species and 104 reactions	Kazakov and Frenklach [9]
DRM19	19 species and 84 reactions	Kazakov and Frenklach [9]
GRI-Mech1.2	30 species and 177 reactions	Smith et al. [10]
USC II	109 species and 784 reactions	Wang et al. [23]
Konnov 0.5	125 species and 1205 reactions	Konnov [24]
Petrova and Williams (2006)	43 species and 235 reactions	Petrova and Williams [25]
Petersen et al. (2007)	115 species and 665 reactions	Petersen et al. [15]
Chen et al. (2007)	43 species and 263 reactions	Chen et al. [27]
Zhao et al. (2008)	52 species and 290 reactions	Zhao et al. [28]
Zsely_50s_186r (2011)	48 species and 186 reactions	Zsely et al. [22]
Zsely_50s_251r (2011)	48 species and 251 reactions	Zsely et al. [22]
Rasmussen et al. (2008)	43 species and 316 reactions	Rasmussen et al. [29]
Huang and Bushe (2006)	52 species and 277 reactions	Huang and Bushe [30]

Some mechanisms, such as Konnov 0.5, had convergence difficulties in the laminar flame speed computation and were not fully evaluated for laminar flame speed. In addition, the detailed mechanism NUIG-NGM_III was not evaluated because its large number of species and reactions (229 species and 1359 reactions) resulted in long computational times (approximately 8 hours computing laminar flame speed with the PREMIX code), and iterations were proven difficult. However, the reduced mechanisms of Zsely were derived directly from the NUIG-NGM III mechanism.

During the development of the MD19 reduced chemical kinetic mechanism, special attention was put on the combination of reduced and detailed mechanisms for hydrocarbons and H_2/O_2 chemistry. The MD19 reduced chemical kinetic mechanism was initially based on the DRM19 reduced methane oxidation mechanism, which was developed by Kazakov and Frenklach [9] by reducing GRI-Mech1.2 down to 19 species and 84 reactions. The relatively small number of species in this mechanism made it a primary candidate as a starting point. The MD19 mechanism was updated with the reaction rate constants and third body efficiencies for hydrocarbon reactions from the Zsely 50s_251 mechanism [22].

These rate constants and efficiencies were chosen because they showed better agreement with the experimental laminar flame speed data at high pressures and lean conditions for the Zsely mechanism [22]. After updating the rate constants for the hydrocarbon reactions, the H_2/O_2 sub-mechanism was modified according to the study of Burke, et al. as it provided the MD19 mechanism with the most current H_2/O_2 high pressure kinetic data. A summary of the process used to arrive to the MD19 improved mechanism is shown in Figure 8.

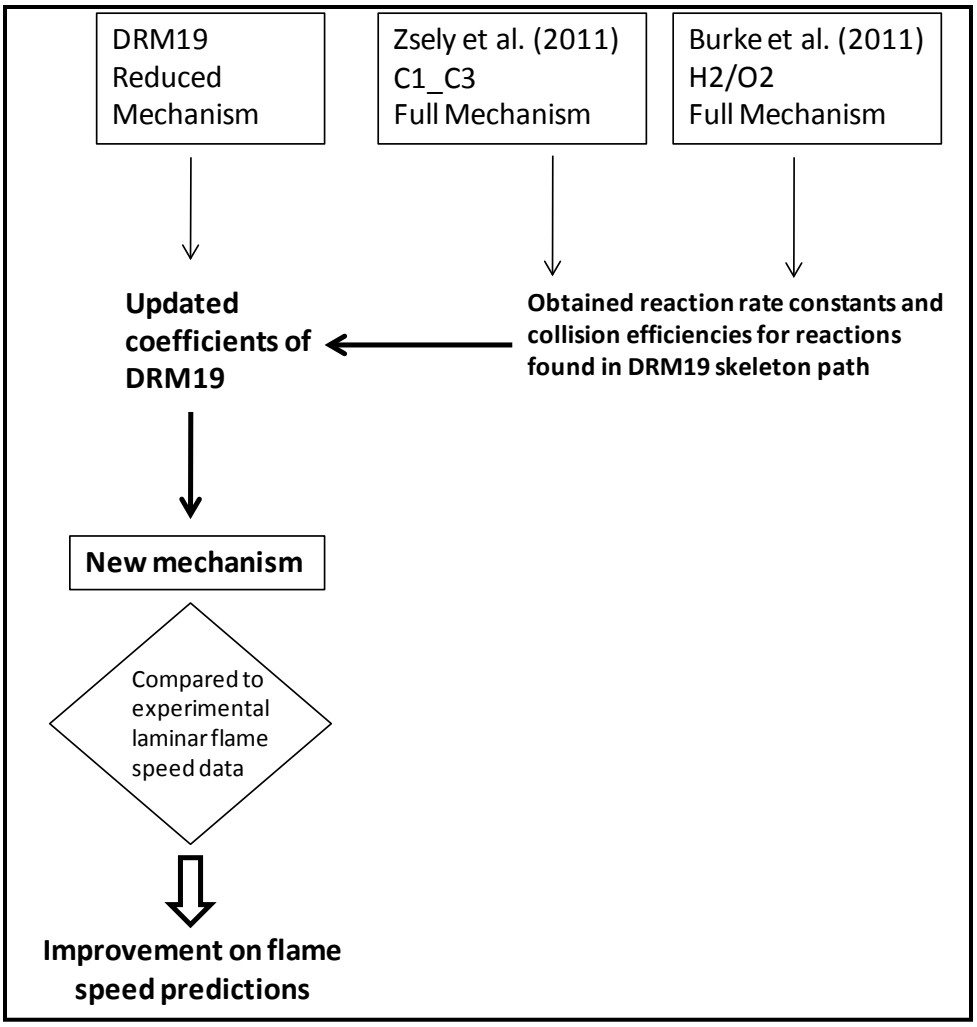

Figure 8. Development path of MD19 kinetic mechanism. The appropriate rate constants from the most accurate mechanisms were used to update the previously reduced DRM19 mechanism.

The resulting MD19 mechanism has 19 species and 84 reactions and is small enough to run engine CFD simulations using commercially available code, such as CONVERGE.

The Nagy21-Burke-MD19 mechanism was developed with collaboration with Dr. Tibor Nagy from the Laboratory of Chemical Kinetics, Eotvos University in Budapest. The SEM (simulation error minimization) mechanism reduction algorithm was used to pare the Zsely [22] reduced mechanisms down to the order of 20 species, using the high pressures and lean conditions typical of high BMEP lean-burn engines. Several reduced mechanisms were provided,

and after identifying the most suitable mechanism for CFD simulation, the rate coefficients of the H_2/O_2 chemistry were updated with the work from Burke et al. [33] and two stiff reactions were later updated with the MD19 mechanism after finding them being too stiff for the CFD solver.

3.1 Flame Speed Analysis

The predicted laminar flame speed values obtained from CHEMKIN PREMIX calculations are presented in Table 4 along with the experimental data for the different pressures and equivalence ratios investigated. Table 4 summarizes the calculated laminar flame speed obtained for the different detailed and reduced chemical kinetic mechanisms. Each mechanism was tested under the four operating conditions for pressure and equivalence ratio presented in Table 1 and compared to those experimental results. In all cases, Zsely 50s_251r, Zsely50s_186r, and the MD19 reduced mechanism closely approach the experimental values of flame speed, having less than 30% error for all the pressure and air/fuel ratio conditions investigated. Conversely, the remaining mechanisms over predict the flame speed considerably. Some mechanisms, like Zhao et al. (2008), were only evaluated at 20 atm, and no further investigation was required based on the inaccuracy of the results.

Table 4. Laminar flame speed calculations for lean methane/air at elevated pressures.

	Mechanism	Number of reactive species and reactions	CHEMKIN Laminar Flame Speed (cm/s)	% Error relative to experimental
5 atm, eq. ratio 0.7	GRI-Mech3.0	51 and 325	7.96	22%
	GRI-Mech1.2	30 and 177	8.80	35%
	DRM22	22 and 104	9.48	46%
	DRM19	19 and 84	9.34	44%
	Zsely et al. (2011) 50s_251r	48 and 251	6.03	7%
	Zsely et al. (2011) 50s_186r	48 and 186	6.10	6%
	USC II	109 and 784	9.46	46%
	Petrova and Williams (2006)	43 and 235	7.89	21%
	MD19	19 and 84	5.98	8%
	Nagy21-Burke-MD19	21 and 58	6.40	2%
5 atm, eq. ratio 0.6	GRI-Mech3.0	51 and 325	4.10	82%
	GRI-Mech1.2	30 and 177	4.04	80%
	DRM22	22 and 104	4.51	100%
	DRM19	19 and 84	4.36	94%
	Zsely et al. (2011) 50s_251r	48 and 251	2.71	20%
	Zsely et al. (2011) 50s_186r	48 and 186	2.74	22%
	USC II	109 and 784	4.83	115%
	Petrova and Williams (2006)	43 and 235	3.63	61%
	Petersen et al. (2007)	115 and 665	4.31	92%
	MD19	19 and 84	2.66	18%
	Nagy21-Burke-MD19	21 and 58	2.40	7%

	Mechanism	Number of reactive species and reactions	CHEMKIN Laminar Flame Speed (cm/s)	% Error relative to experimental
10 atm, eq. ratio 0.7	GRI-Mech3.0	51 and 325	5.32	33%
	GRI-Mech1.2	30 and 177	5.61	40%
	DRM22	22 and 104	6.20	55%
	DRM19	19 and 84	5.91	48%
	Zsely et al. (2011) 50s_251r	48 and 251	3.78	6%
	Zsely et al. (2011) 50s_186r	48 and 186	3.81	5%
	USC II	109 and 784	6.03	51%
	Petrova and Williams (2006)	43 and 235	5.16	29%
	Petersen et al. (2007)	115 and 665	5.57	39%
	MD19	19 and 84	3.85	4%
	Nagy21-Burke-MD19	21 and 58	3.40	15%
20 atm, eq. ratio 0.7	GRI-Mech3.0	51 and 325	3.84	92%
	GRI-Mech1.2	30 and 177	3.49	75%
	DRM22	22 and 104	3.90	95%
	DRM19	19 and 84	3.55	78%
	Zsely et al. (2011) 50s_251r	48 and 251	2.40	20%
	Zsely et al. (2011) 50s_186r	48 and 186	2.41	21%
	Petrova and Williams (2006)	43 and 235	3.46	73%
	Petersen et al. (2007)	115 and 665	3.40	70%
	Chen et al. (2007)	43 and 263	3.71	86%
	Zhao et al. (2008)	52 and 290	3.50	75%
	Rasmussen et al. (2008)	43 and 316	3.14	57%
	Huang and Bushe (2006)	52 and 277	3.52	76%
	MD19	19 and 84	2.58	29%
	Nagy21-Burke-MD19	21 and 58	1.90	5%

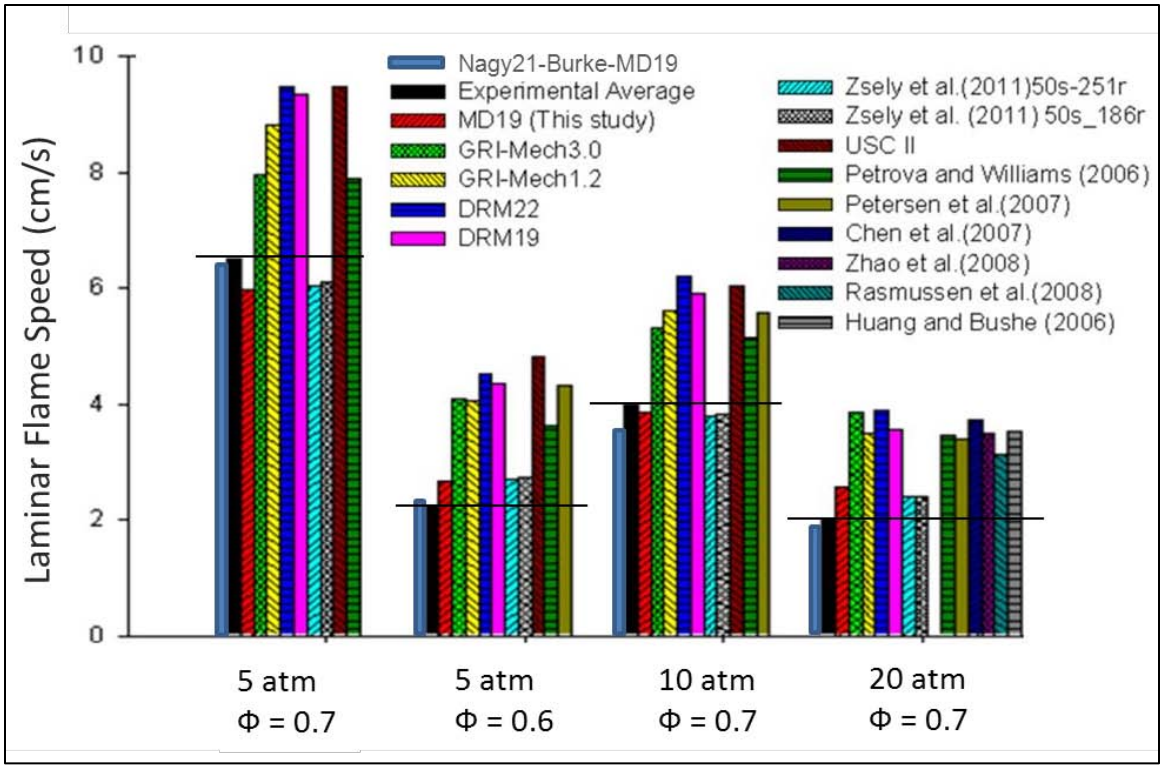

Figure 9. Laminar flame speed calculations for lean methane/air at elevated pressures as presented in Table 4.

The laminar flame speed results from the different mechanisms and the experimental data presented in Table 4 are shown in a bar chart in Figure 9. The MD19 and Nagy21-Burke-MD19 mechanisms are in good agreement with the experimental data and with other larger mechanisms. Also included in Table 4 is the accuracy of the different chemical kinetic mechanisms in terms of percent deviation from the experimental measurements. It can be seen that detailed mechanisms such as GRI-Mech3.0 and USC-II over predict the laminar flame speed by as much as 100% under these conditions. The reduced mechanisms such as DRM22 and DRM19 behave similarly.

3.2 Chemical Kinetics and Pressure Dependent Reactions

As in the reduced chemical kinetic mechanisms from this work, most of the reactions of interest in the combustion field are bimolecular. In this type of reaction, two molecules collide and react to form two different molecules.

$$A+B \rightarrow C + D \qquad (7)$$

In these detailed mechanisms, the oxidation process of a fuel molecule is described with transitional steps in which intermediate species are formed. There are many different types of elementary reactions and they are categorized depending on the number of molecules involved, and the interaction they play in the overall reaction path. Examples of such reactions are unimolecular, bimolecular, termolecular, which depend on number of molecules; chain (with chain-initiation, propagation, and termination reactions), chain-branching, which determine the course of the reaction.

In addition to the rate constants for the forward and reverse (REV) steps specified in each reaction, there are additional reaction rate constants to be used depending on the pressure dependence of specific reactions, this allows for transition in the computation when the combination of the high and low pressure limits is approached. An example of these expressions is presented in Figure 10, next page. The “LOW” expression corresponds to the coefficients that represent the high-pressure limit behavior. With the specified parameters under “HIGH”, the coefficients given in the reaction line represent the low-pressure limit behavior. If the reaction is in between the high and low pressure limits, the reaction is known as “fall-off reaction” and special methods to represent the rate expressions are needed. Two of these forms are known as the Lindemann and the TROE expressions and they provide with a solution for the rate constants at the pressure fall-off limits. When a reaction rate cannot be described by a single Arrhenius form, more than one set can be provided and in that case, the parameter “DUP” indicates the

reaction is declared as a duplicate and the sum of the set of rates will be used.

The interesting pressure dependence of unimolecular reactions involving “third body” (referred as M) collisions, can be explained by an example using the methyl radical recombination reaction as written in CHEMKIN format and presented in Figure 10.

Reaction	A (cm-mol-s)	b	E_a cal/mol
$H+CH_2(+M)\leftrightarrow CH_3(+M)$	0.500E+16	-0.800	0.00
LOW	3.200E+27	-3.140	1230.00
TROE	0.6800 78.00	1995.00	5590.00
ηH_2=2.00/ ηH_2O=6.00/ ηCH_4=2.00/ ηCO=1.50/ηCO_2=2.00/ ηC_2H_6=3.00/ ηAR=0.70			

Figure 10. Reaction extract from MD19 mechanism in CHEMKIN format.

Making reference to the reaction in Figure 10, at the high pressure limit, the proper representation of the reaction is

$$H+CH_2 \leftrightarrow CH_3 \quad (8)$$

and at the low pressure limit, the concentration of third body molecule (M) greatly affects the collision for the reaction to proceed in the path:

$$CH_3 + M \rightarrow_{k1} CH_2 + H + M \quad (9)$$

$$CH_2 + H + M \rightarrow_{k2} CH_3 + M \quad (10)$$

If the pressure conditions are such that the reaction is between the high/low pressure limits, the “fall-off” expression is used by writing the third body concentration with a parenthesis in the mechanism (+M) as presented in Figure 10.

At the initial point (equation 9), the methyl radical collides with a third body and brakes into CH_2 + H as a result. After this, two different processes may happen: CH_2 + H may collide with another molecule (third body) resulting in the formation of CH_3, or on the other hand, the

radicals H + CH_2 may react with other molecules forming different products.

$$CH_2+H \rightarrow_{k3} \text{ Products} \qquad (11)$$

To understand the pressure dependence in this reaction, a function of the overall reaction rate needs to be found. In this example, the rate at which products are formed in reaction (11) is

$$\frac{d[Products]}{dt} = k_3[CH_2][H] \qquad (12)$$

Using the steady-state approximation, the net production of CH_2+H can be expressed as

$$\frac{d[CH_2][H]}{dt} = k_1[CH_3][M] - k_2[CH_2][H][M] - k_3[CH_2][H] \qquad (13)$$

By taking that d[CH_2][H]/dt=0 under the steady state assumption, and solving for [CH_2][H] results in:

$$[CH_2][H] = \frac{k_1[CH_3][M]}{k_2[M]+k_3} \qquad (14)$$

substituting equation (12) into (14) results in

$$\frac{d[Products]}{dt} = \frac{k_3k_1[CH_3][M]}{k_2[M]+k_3} = \frac{k_1[CH_3][M]}{k_2/k_3[M]+1} \qquad (15)$$

For the overall reaction:

$$CH_3 \rightarrow_{kuni} \text{ Products} \qquad (16)$$

where K_{uni} is the apparent unimolecular rate coefficient, the rate of CH_3 transformation can be written as:

$$-\frac{d[CH3]}{dt} = \frac{d[Products]}{dt} = k_{uni}[CH_3] \qquad (17)$$

The apparent unimolecular rate coefficient can be found by combining equations (15) and (17):

$$k_{uni} = \frac{k_1[M]}{k_2/k_3[M]+1} \qquad (18)$$

By analyzing equation (18), the pressure dependence of the combined reactions (9) and (10) can be explained as follows: at elevated pressures, the concentration of M increases; and at high enough pressures, the term $(k_2/k_3)[M]$ becomes much larger than unity, and consequently

the [M] term of the numerator and denominator cancel each other resulting in:

$$k_{uni}(P \to \infty) = \frac{k_1 k_3}{k_2} \qquad (19)$$

At low enough pressures, the term $(k_2/k_3)[M]$ is much less than unity and can be neglected, the resulting form of equation (18) is then:

$$k_{uni}(P \to 0) = k_1[M] \qquad (20)$$

4. REACTION PATH ANALYSIS

To better understand the structure of the main chemical kinetic mechanisms discussed in this work, a reaction path analysis was carried using CHEMKIN-PRO during the computation of flame speeds at 20 atm and equivalence ratio of 0.7. This examination was carried out by selecting a sensitivity analysis on methane and by calculating the reaction path ahead of the adiabatic flame temperature position, between the unburnt gas region and the burnt gas region. As Figure 11 shows, the grid point selection for the analysis was an intermediate temperature between the ambient gas of the premixed CH_4/Air mixture and the corresponding adiabatic flame temperature at 20 atm and equivalence ratio of 0.7. This grid location was kept constant for the analysis of the mechanisms presented in this section.

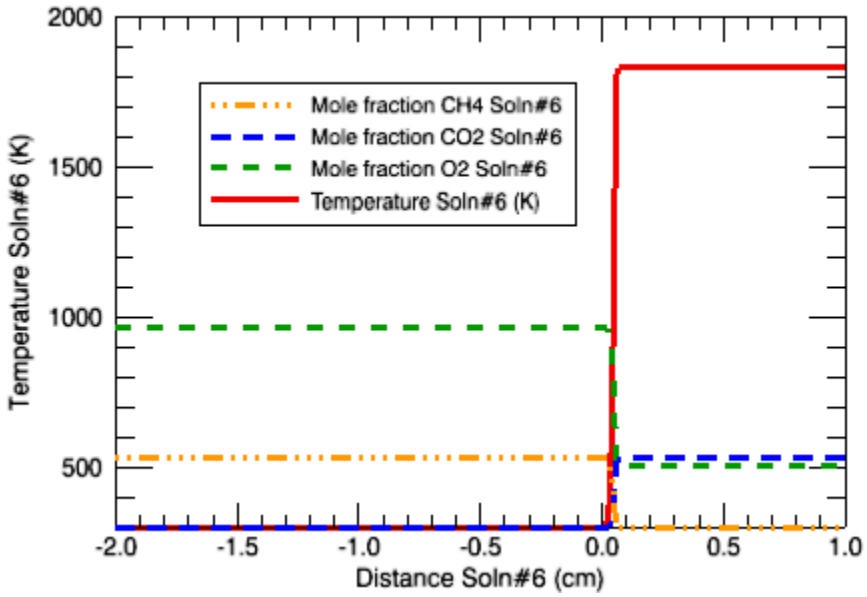

Figure 11. Selected flame position for reaction path analysis. Analysis on Zsely_50s_251r mechanism. (species mole fractions not at scale). Figure obtained from CHEMKIN.

At the selected conditions, the methane oxidation is already taking place, as indicated by the concentration of intermediate species and products of combustion. However, must of the fuel mass is still present for the analysis of methane oxidation.

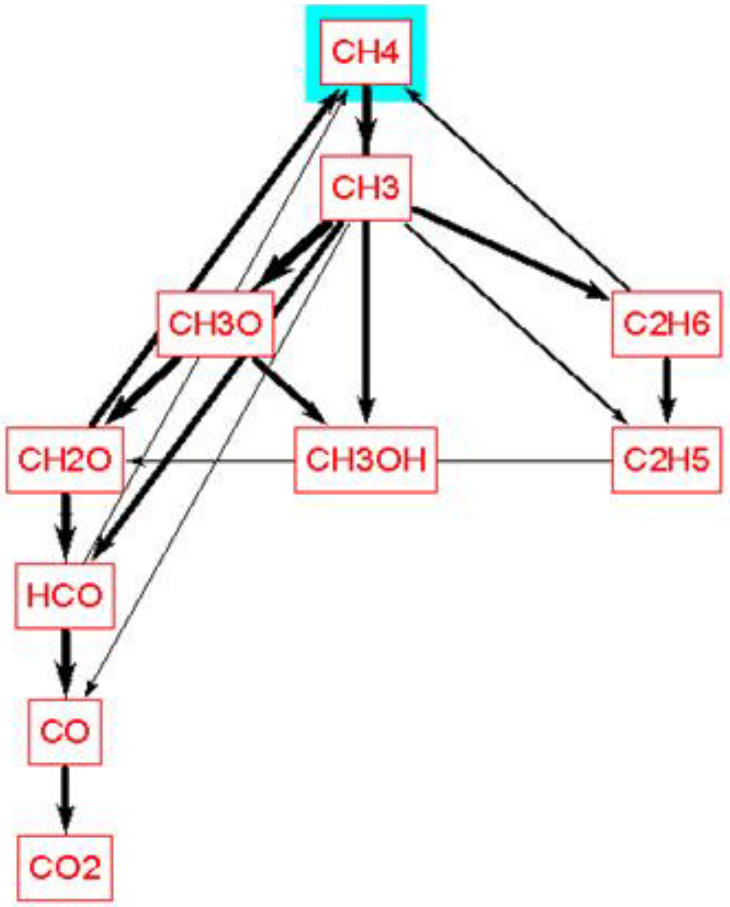

Figure 12. Reaction path analysis for GRI-Mech3.0. Figure obtained from CHEMKIN.

The reaction path analysis GRI-Mech3.0 presented in Figure 12 represents a hierarchical sensitivity analysis to the CH_4 combustion. The figure only shows the 10 most important species containing carbon atoms. The preignition chemistry of methane is dictated by the rate of radical accumulation, and depending on the thermodynamic conditions, the initial chain reactions are initiated by either:

$$CH_4+M \leftrightarrow CH_3+H+M \qquad (21)$$

$$CH_4+O_2 \leftrightarrow CH_3+HO_2 \qquad (22)$$

Reaction (21) has a large activation energy, 1.39×10^{16} cal/mol, and it is favored over (22) that has an activation energy of 1×10^{12} cal/mol, at high temperatures only (>1500 K). At high

temperatures, the dominant reactions that follow are:

$$H+O_2 \leftrightarrow OH+O \qquad (23)$$

$$CH_4 + (H,O,OH) \leftrightarrow CH_3 + (H_2, OH, H_2O) \qquad (24)$$

When reaction (23) dominates the initiation step, the radical pool growth is followed by reactions:

$$CH_4+HO_2 \leftrightarrow CH_3+H_2O_2 \qquad (25)$$

$$H_2O_2+M \leftrightarrow OH+OH+M \qquad (26)$$

Figure 12 shows the initial radical formation of CH_3 as the unique initiation path for the decomposition of methane at the selected conditions. This is indicated by the black arrow that points into the CH_3. In the figure, the arrow thickness indicates the preferred path for the reaction progress. Once the pool of CH_3 radicals is formed, the progress goes into six possible paths: formation of CH_3O, C_2H_6, CH_3OH, HCO, C_2H_5, or the least preferred, the direct formation of CO without an intermediate step. After the initial radical formation, the oxidation of fuel radicals takes place through a linear path going from CH_2O, to HCO and CO until the final product for carbon atoms, CO_2 molecule. During this process, some reverse reactions occur that result in the production of CH_4, like in the reactions:

$$CH_3+CH_3(+M) \leftrightarrow C_2H_6(+M) \qquad (27)$$

$$HO_2+CH_3 \leftrightarrow O_2+CH_4 \qquad (28)$$

Reactions (27) and (28) are radical termination steps, which inhibits ignition.

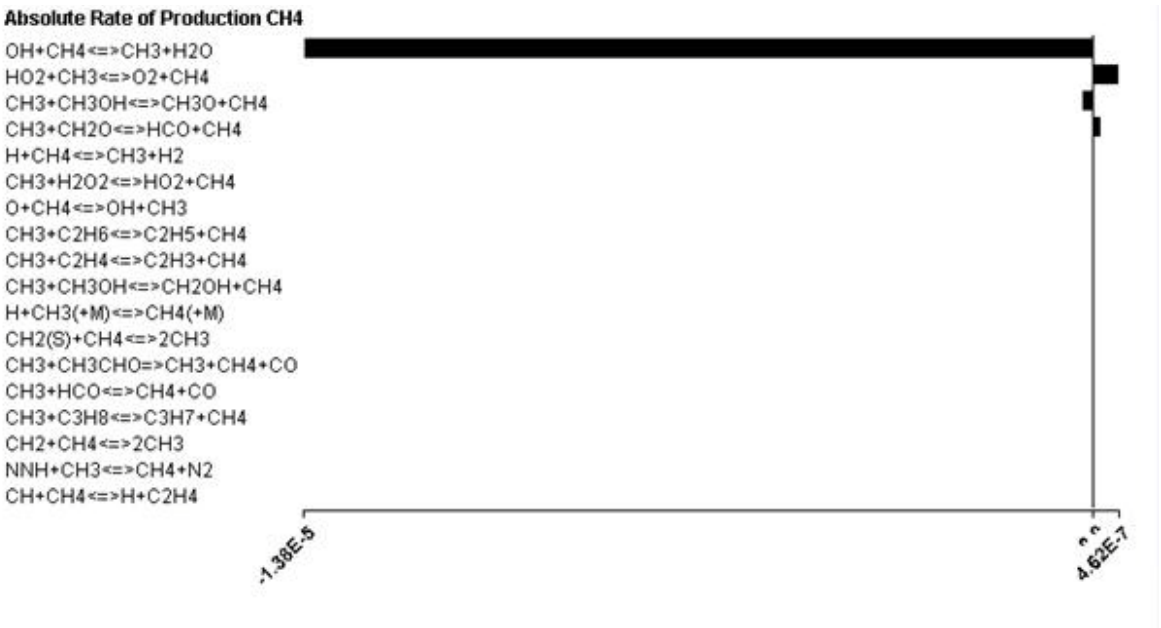

Figure 13. Rates of production of all reactions that influence the CH_4 equilibrium at the selected solution point for GRI-Mech3.0. Figure obtained from CHEMKIN.

Figure 13 shows the most sensitive reactions that affect methane combustion at the selected conditions. The negative rate of production indicates CH_4 breakup, as in the first reaction $OH+CH_4 \leftrightarrow CH_3+H_2O$. While the positive rate of production indicates CH_4 formation as in the reaction $HO_2+CH_3 \leftrightarrow O_2+CH_4$. As the magnitude of the bar shows, the first four reactions at the top are the most influential in the rate of CH_4 production, and the main channel for CH_4 breakup is through the attack of OH radicals to the methane molecule, creating CH_3 radicals and H_2O. As can be seen in the rest of the reactions from the figure, the CH_3 radical is involved in most of them.

Figure 14. Sensitivity of selected species in relation to the rates of reactions of the mechanism for GRI-Mech3.0. Figure obtained from CHEMKIN.

The normalized sensitivity analysis from Figure 14 indicates how each reaction rate coefficient affects the CH_4 equilibrium (and the temperature and species profiles) at the specified point in the flame. The negative magnitude of the sensitivity indicates the path of fuel depletion; and the positive magnitude indicates termination steps for intermediate radicals, or fuel formation. The two most important reactions, as indicated by their magnitudes, are the formation of OH radical trough $H+O_2 \leftrightarrow O+OH$ and $HO_2+CH_3 \leftrightarrow OH+CH_3O$. As presented in Figure 13, the OH radical is responsible for most of the initial CH4 breakup during the combustion process of the flame at the specified point. Reactions that compete with the fuel oxidation by decreasing the concentration of reactive radicals and creating more stable ones, such as $H+O_2+H_2O \leftrightarrow HO_2+H_2O$; $OH+HO_2 \leftrightarrow O_2+H_2O$; $H+CH_3(+M) \leftrightarrow CH_4(+M)$; $2CH_3(+M) \leftrightarrow C_2H_6(+M)$; and $2HO_2 \leftrightarrow O_2+H_2O_2$.

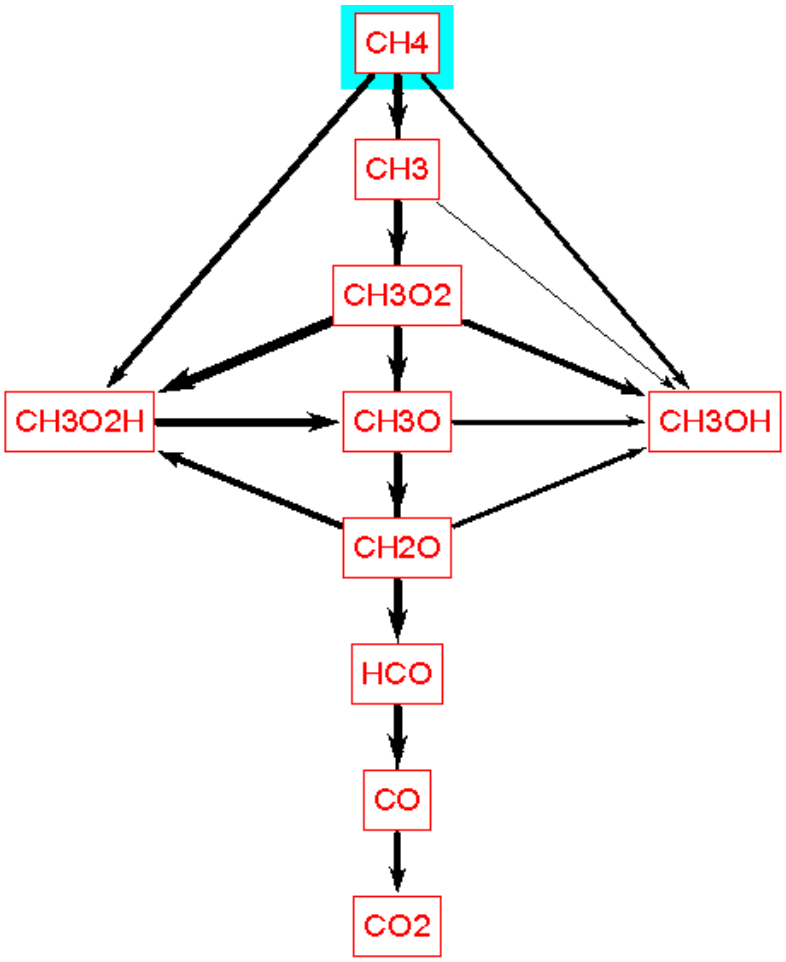

Figure 15. Reaction path analysis for Zsely 50s 251rxn. Figure obtained from CHEMKIN.

Figure 15 shows the reaction path for the Zsely 50s 251r mechanism at the same conditions as presented for GRI-Mech3.0 mechanism (20 atm, $\phi = 0.7$, and flame location at 760 K). The initial decomposition of the CH_4 molecule during oxidation leads to the production of CH_3, CH_3O_2H, and CH_3OH. The combustion then proceeds to a "competence" time where formation of small partially oxidized molecules (CH_3O and CH_2O) competes with the formation of larger intermediate species such as CH_3O_2H and CH_3OH. The final steps for the CH_4 fortune consists of the linear steps of intermediate species formation $CH_2O \rightarrow HCO \rightarrow CO \rightarrow CO_2$ until the final product for carbon atoms CO_2 is formed.

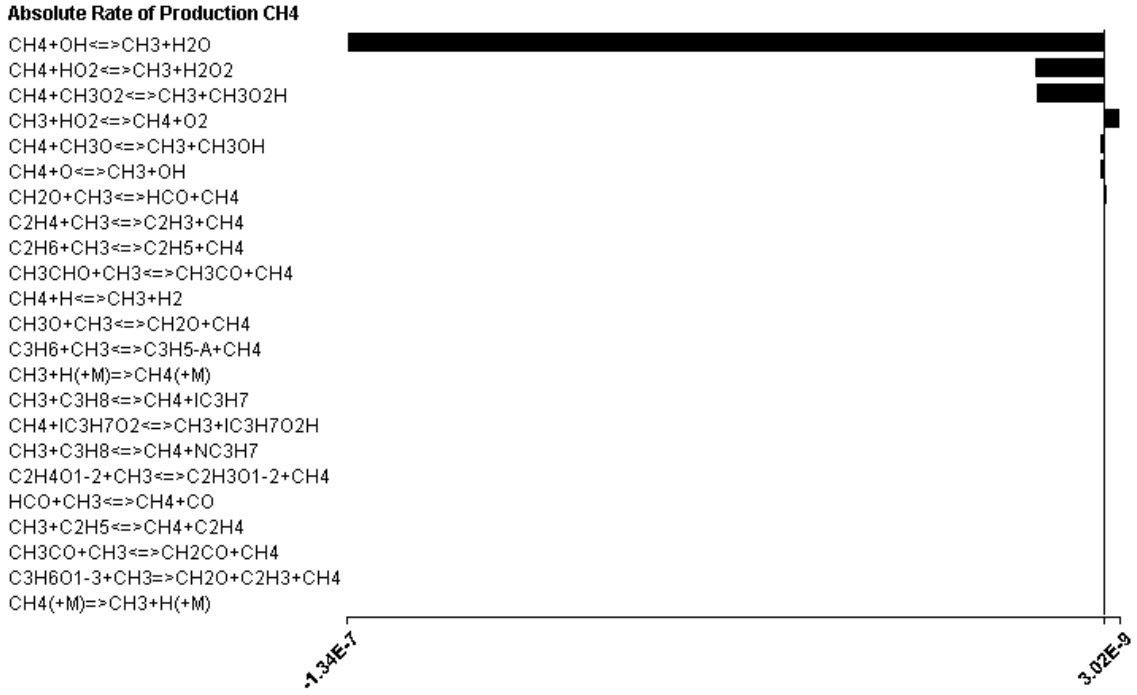

Figure 16. Rates of production of all reactions that influence the CH_4 equilibrium at the selected solution point for Zsely 50s 251rxn. Figure obtained from CHEMKIN.

The rate of production of the most dominant reactions in methane combustion modeled by the Zsely 50s 251rxn are presented in Figure 16. The main initiation step is the collision of the OH radical with the fuel, CH_4, for the formation of CH_3 and H_2O. The other two species that directly attack the fuel molecule the most are HO_2 and CH_3O_2 radicals as shown by the second and third reactions from the top. The reaction that competes with the oxidation process the most is $CH_3+HO_2 \leftrightarrow CH_4+O_2$. This reaction combines two radicals to produce the original fuel and oxygen molecules.

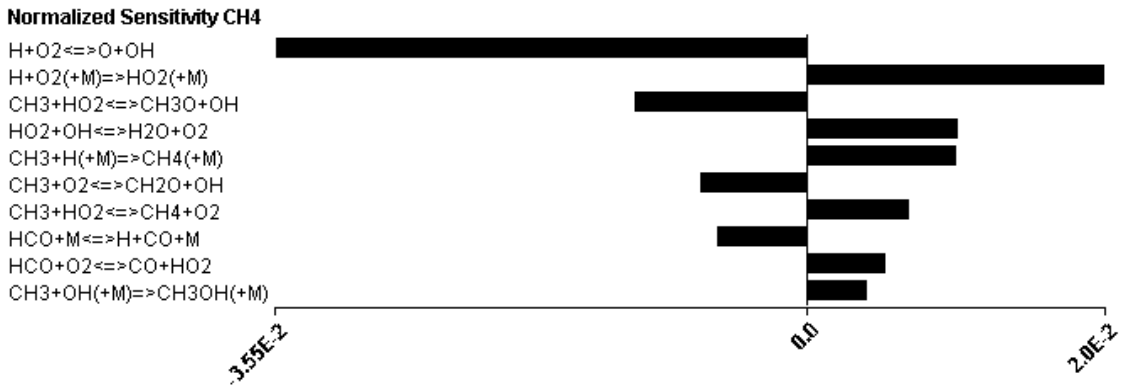

Figure 17. Sensitivity of selected species in relation to the rates of reactions of the mechanism for Zsely 50s 251rxn. Figure obtained from CHEMKIN.

Figure 17 shows the sensitivity of the most dominant reactions affecting the overall combustion process modeled by the Zsely 50s 251r mechanism. The reaction $H+O_2 \leftrightarrow O+OH$ dominates the oxidation process closely followed by competition reactions involving radical termination steps like $H+O_2(+M) \rightarrow HO_2(+M)$; $HO_2+OH \leftrightarrow H_2O+O_2$; and reactions that contribute to fuel oxidation such as $CH_3+HO_2 \leftrightarrow CH_3O+OH$.

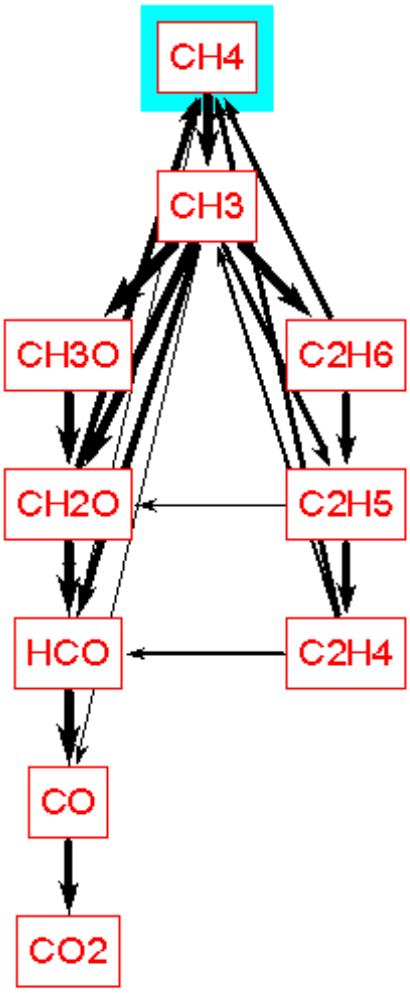

Figure 18. Reaction path analysis for DRM22 mechanism. Figure obtained from CHEMKIN.

The structure of the methane combustion reaction path as modeled by the DRM22 mechanism presents more ramification in the sequence of intermediate species formation, and a more average weighted probability of the reaction path as the similar arrow thickness of Figure 18 indicate. The initial step as modeled by DRM22 is the formation of CH_3 radicals. From there, the path taken by the mechanism is divided in termination steps involving C_2H_6, C_2H_5, C_2H_4 species formation, or chain propagation reactions that reduce the molecule size from CH_3O down to CH_2O, HCO, CO and finally CO_2.

Figure 19. Rates of production of all reactions that influence the CH_4 equilibrium at the selected solution point for DRM22. Figure obtained from CHEMKIN.

Figure 19 shows the absolute rate of production of CH_4 throughout the reaction path. As indicated by its magnitude, the reaction $OH+CH_4 \leftrightarrow CH_3+H_2O$ dominates the methane combustion process. The burning rate of methane is decreased by the competing reaction $HO_2+CH_3 \leftrightarrow O_2+CH_4$.

Figure 20. Sensitivity of selected species in relation to the rates of reactions of the mechanism for DRM22. Figure obtained from CHEMKIN.

The reactions that have more effect in the fuel oxidation are $H+O_2 \leftrightarrow O+OH$, and $HO_2+CH_3 \leftrightarrow OH+CH_3O$ which accounts for most of the OH radical, key in the radical pool formation that attack the fuel molecules.

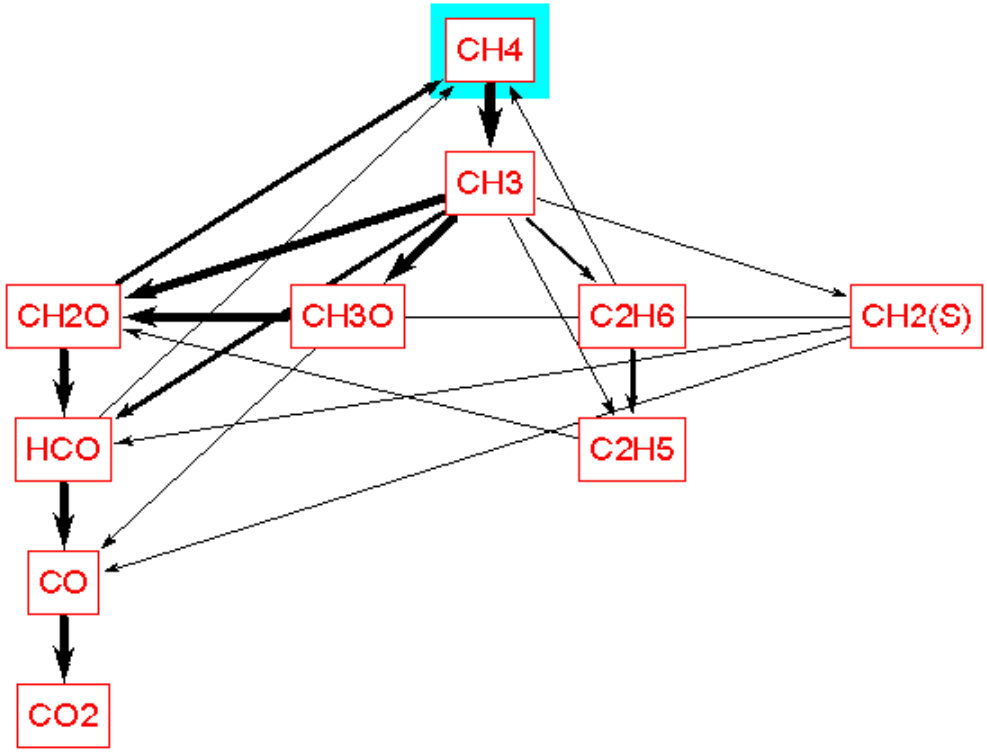

Figure 21. Reaction path analysis for MD19. Figure obtained from CHEMKIN.

The reaction path of the MD19 mechanism once again shows the formation of CH_3 as the initial step, followed by competing reactions that affect the equilibrium of CH_4 concentration. The pattern is similar to the previous mechanisms with a competition between interactions formatting intermediate species $CH_{2(S)}$, CH_3O, C_2H_6, C_2H_5, and CH_2O that with a lesser impact slows down the methane burning rate; and the more straightforward steps from $CH_2O \rightarrow HCO \rightarrow CO \rightarrow CO_2$

Figure 22. Rates of production of all reactions that influence the CH_4 equilibrium at the selected solution point for MD19. Figure obtained from CHEMKIN.

The sensitivity to rate of CH_4 production is presented in Figure 22. Once again, the most important reaction is the OH attack on the fuel molecule, $CH_4+OH \leftrightarrow CH_3+H_2O$.

Figure 23. Sensitivity of selected species in relation to the rates of reactions of the mechanism for MD19. Figure obtained from CHEMKIN.

Figure 23 shows the normalized sensitivity to CH_4 combustion at the flame front. The hydrogen/oxygen chemistry shows its importance in combustion once again with the OH radical pool formation trough $H+O_2 \leftrightarrow O+OH$; with competing reactions that deplete radicals, namely the reactions: $HO_2+OH \leftrightarrow H_2O+O_2$, and $H+O_2(+M) \rightarrow HO_2(+M)$.

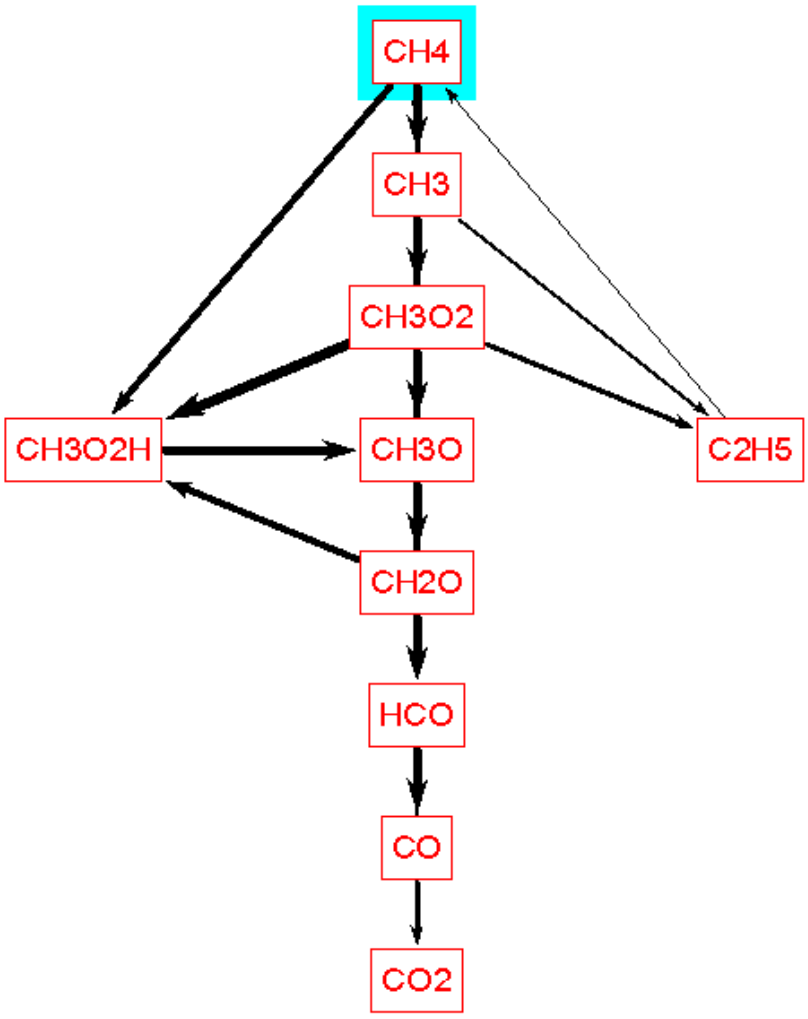

Figure 24. Reaction path analysis for Nagy21. Figure obtained from CHEMKIN.

The initial CH_4 breakup as modeled by the Nagy21 mechanism shows initial species formation between CH_3 (mainly) and CH_3O_2H. Intermediate equilibrium balancing reactions occur forming the species CH_3O_2, C_2H_5, CH_3O, and CH_2O. The final steps described by the Nagy21 mechanism is the sequence of reactions forming $CH_2O \rightarrow HCO \rightarrow CO \rightarrow CO_2$.

Figure 25. Rates of production of all reactions that influence the CH_4 equilibrium at the selected solution point for Nagy21. Figure obtained from CHEMKIN.

The absolute rate of CH_4 production as presented in Figure 25 indicates that the reaction $CH_4+OH\leftrightarrow CH_3+H_2O$ is the dominant reaction in the CH_4 breakdown followed by the reactions $CH_4+HO_2\rightarrow CH_3+H_2O_2$, and $CH_4+CH_3O_2\rightarrow CH_3+CH_3O_2H$.

Figure 26. Sensitivity of selected species in relation to the rates of reactions of the mechanism for Nagy21. Figure obtained from CHEMKIN.

Figure 26 shows the normalized sensitivity for CH_4 combustion, and indicates that the reaction responsible for providing most of the OH radicals is $H+O_2\leftrightarrow O+OH$ followed by $CH_3+HO_2\rightarrow CH_3O+OH$. In the Nagy21 mechanism, the H radical is responsible for the initial oxygen, O_2, recombination, and this H radical concentration is equilibrated with the reaction $H+O_2(+M)\leftrightarrow HO_2(+M)$ that in presence of a third body reaction, it consumes the H radical and

creates the less reactive molecule HO_2, instead of the hydroxyl radical as in the top reaction from Figure 26

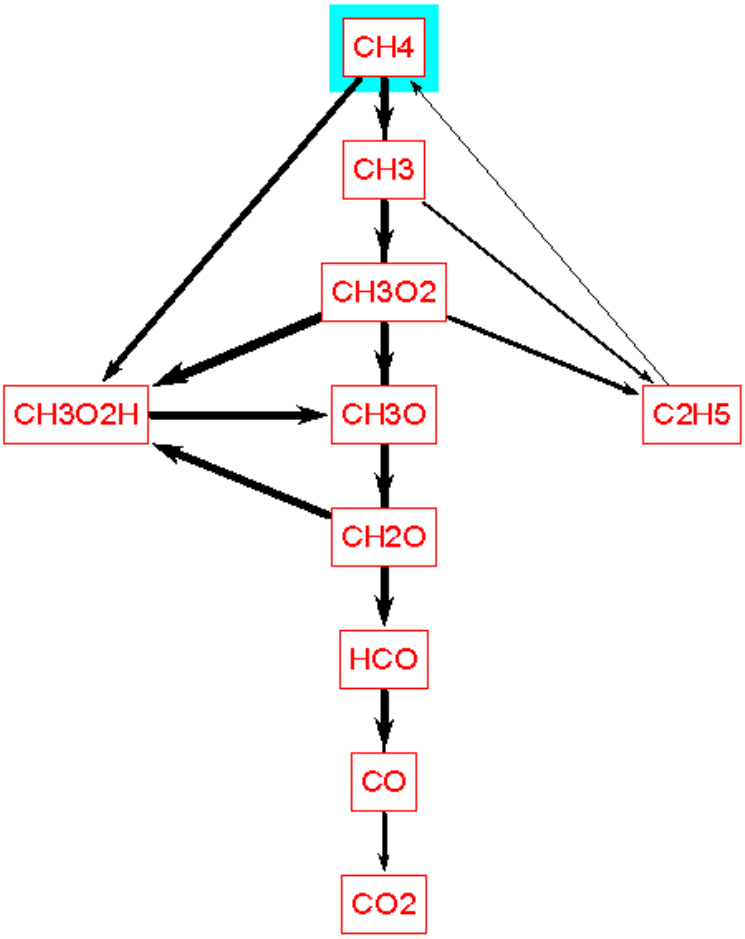

Figure 27. Reaction path analysis for Nagy21-Burke-MD19. Figure obtained from CHEMKIN.

The reaction path for the Nagy21-Burke-MD19 mechanism is presented in Figure 27. The initial CH_4 breakdown produces CH_3 and CH_3O_2H radicals. The reaction path then proceeds to equilibrium with forward and backward reactions involving the species CH_3O_2H, CH_3O_2, CH_3O, C_2H_5, and CH_2O. The final steps in the mechanism follow the straight path from CH_2O, to HCO, CO and the final product CO_2.

Figure 28. Rates of production of all reactions that influence the CH_4 equilibrium at the selected solution point for Nagy21-Burke-MD19. Figure obtained from CHEMKIN.

The absolute rate of CH_4 production as modeled by the Nagy21-Burke-MD19 is presented in Figure 28. The dominant reaction affecting CH_4 is $CH_4+OH \leftrightarrow CH_3+H_2O$, followed by $CH_4+CH_3O_2 \rightarrow CH_3+CH_3O_2H$, and $CH_4+HO_2 \rightarrow CH_3+H_2O_2$.

Figure 29. Sensitivity of selected species in relation to the rates of reactions of the mechanism for Nagy21-Burke-MD19. Figure obtained from CHEMKIN.

Figure 29 shows the normalized sensitivity to the combustion mechanism involving methane. The reaction $H+O_2 \leftrightarrow O+OH$ is responsible for providing most of the OH radicals that attack the CH_4 molecule, and is balanced by the radical termination reactions such as $H+O_2(+M) \leftrightarrow HO_2(+M)$.

From the analysis presented in this section, and thanks to the recent progress in combustion science, a better understanding of detailed reaction mechanisms for hydrocarbon

oxidation is now possible. According to the most general consensus [39], one of the most important reactions in combustion is considered to be:

$$H+O_2 \rightarrow O+OH \qquad (29)$$

This reaction is independent of the initial fuel molecule size, and it shows the importance of the basic hydrogen/oxygen chemistry in hydrocarbon combustion. As presented in this section, reaction (29) shows up as the most sensitive reaction normalized with respect to CH_4 for all the mechanisms presented, showing the importance of the H_2/O_2 chemistry in the combustion kinetic mechanisms of this work.

Table 5 presents a summary of the most important reactions responsible for CH_4 oxidation (after reaction 29 being the most sensitive to fuel consumption for all mechanisms) based on the sensitivity analysis of this section.

Table 5. Summary of the most sensitive reactions responsible for CH_4 oxidation according to the Reaction Path Analysis.

Analysis	**Reaction**	**Present in Mechanism**
Normalized Sensitivity to CH_4	$CH_3+HO_2 \rightarrow CH_3O+OH$	Nagy21-Burke-MD19, Nagy21, DRM22, Zsely50s_251rxn, GRI-Mech3.0
	$CH_3+O_2 \rightarrow CH_2O+OH$	MD19
Absolute Rate of Production to CH_4	$CH_4+OH \rightarrow CH_3+H_2O$	Nagy21-Burke-MD19, Nagy21, MD19, Zsely50s_251rxn, DRM22, GRI-Mech3.0

The most important reactions responsible for radicals consumption, or reverse reactions that produce CH_4 are presented in Table 6.

Table 6. Summary of the most sensitive reactions responsible for radical consumption, or reverse reactions that produce CH_4 according to the Reaction Path Analysis.

Analysis	**Reaction**	**Present in mechanism**
Normalized Sensitivity to CH_4	$H+O_2(+M) \rightarrow HO_2(+M)$	Nagy21-Burke-MD19, Nagy21, Zsely50s_251rxn
	$HO_2+OH \rightarrow H_2O+O_2$	MD19, DRM22
	$H+O_2+H_2O \rightarrow HO_2+H_2O$	GRI-Mech3.0
Absolute Rate of Production to CH_4	$CH_3+HO_2 \rightarrow CH_4+O_2$	Nagy21-Burke-MD19, MD19, DRM22, Zsely50s_251rxn, GRI-Mech3.0, Nagy21

From this summary it can be concluded that the key initial step in the breakdown of the methane molecule for all of the analyzed kinetic mechanisms is:

$$CH4+OH \rightarrow CH3+H2O \qquad (30)$$

recalling that reaction (29) is the most important reaction for all of the mechanisms, a connection can be made with reaction (30) as it provides the OH radical for the initial CH_4 oxidation step.

5. VALIDATION RESULTS AND DISCUSSION

After developing this MD19 reduced mechanism, computations of laminar flame speed were performed using CHEMKIN to assess its accuracy at high pressure, lean conditions in comparison to the other mechanisms listed in Table 3. This validation was only performed on lean methane/air mixtures at elevated pressures. Table 7 shows the results of ignition delay performance on the selected reduced mechanisms. The Zsely_50s_251r mechanism was obtained by means of a mechanism reduction method, starting from the NUIG NGM_III mechanism and can be used as a reference to compare the performance of the mechanisms listed in Table 7. The Zsely_50s_251r mechanism was validated using experimental ignition delay data measured for methane/propane mixtures from lean to stoichiometric ($0.5 \leq \phi \leq 1$), at temperatures in the range of 877 – 1465 K and pressures from 7 – 40 atm, from rapid compression machine and shock tube experiments [22].

Table 7. Results of flame speed and ignition delay for selected reduced mechanisms. Calculation performed in CHEMKIN.

Mechanism	Pressure (atm)	Equivalence Ratio Φ	Computed Laminar Flame Speed (cm/s)	Ignition Delay (s)
MD19	20	0.7	2.6	4.9
	10	0.7	3.9	8.5
	5	0.7	6.0	14.4
	5	0.6	2.7	15.7
Nagy21-Burke-MD19	20	0.7	1.9	0.079
	10	0.7	3.4	0.170
	5	0.7	6.4	0.400
	5	0.6	2.4	0.428
Nagy21	20	0.7	2.6	0.088
Nagy23	20	0.7	3.1	NA
Nagy24	20	0.7	3.5	NA
Nagy29	20	0.7	3.5	NA
Zsely_50s_251r	20	0.7	2.4	0.100
	10	0.7	3.8	0.210
	5	0.7	6.0	0.480
	5	0.6	2.7	0.520

As Table 7 demonstrates, the ignition delay for the MD19 mechanism is significantly higher than the other mechanisms. For example, at 20 atm the MD19 predicts an ignition delay of 4.9 seconds compared to 0.1 seconds as predicted by the Zsely_50s_251r mechanism (49 times longer). The Nagy21 mechanism was selected as the optimum mechanism for CFD thanks to its accuracy and for being the smaller in size. This Nagy21-Burke-MD19 mechanism was run without modifications in the CFD program, however, a convergence error was stopping the CFD simulation from completing, causing it to crash. The thermodynamic file supplied in the CHEMKIN and CFD codes contains the heat capacity, enthalpy, and entropy of each species in the form of polynomial fits to temperature. This information was correct, and since there are no fractional stoichiometric coefficients in the mechanisms of this study, the remaining option was to find the reaction or reactions that had a stiff response to the pressures and temperatures tested

in the CFD case.

A direct comparison between the calculated laminar flame speed from the DRM22 mechanism and the MD19, along with experimental data, is shown in Table 8. It can be seen that the DRM22 overestimates the experimental flame speed by a 73% average, while the MD19 mechanism overestimates the experimental flame speed by only a 15% average.

Table 8. Direct comparison of DRM22 and the MD19. The percent deviation from experimental values is shown in parentheses.

P (atm)	ϕ	Experimental Average (cm/s)	DRM22 (cm/s)	MD19 (cm/s)
5	0.7	6.5	9.5 (46%)	6.0 (8%)
5	0.6	2.3	4.5 (96%)	2.7 (17%)
10	0.7	4.0	6.2 (55%)	3.9 (3%)
20	0.7	2.0	3.9 (95%)	2.6 (30%)

5.1 CFD Engine Simulation Results

To validate the improvement offered by the MD19 mechanism, compared to the DRM22, a CFD simulation of a representative natural gas engine was conducted using the CONVERGE simulation program. The results obtained by the simulations were then compared to measured combustion performance from this engine. The engine selected was the Caterpillar G3516C located at the Engine and Energy Conversion Laboratory (EECL) of the Colorado State University (CSU) (see Figure 30). This engine is representative of the state of the art for lean-burn, high efficiency gas engines and it is equipped with an OEM passive prechamber spark plug. The selection of a combustion system with a passive prechamber spark plug was intentionally chosen to validate the "MD19" mechanism with a flame jet type of ignition system which has been proved to be the enabling technology for the future high efficiency, low emissions, lean-burn gas engines. The operating conditions used during the actual engine test and also for the CFD simulation were 1800 rpm, 1.0 g/bhp-hr NOx emissions at 1.5MW.

Figure 30. Caterpillar G3516C engine at the CSU-EECL.

Shown in Figure 31 is a cross sectional view of the Prometheus “virtual” engine used to approximate the combustion geometry of the CAT G3516C engine for the CFD simulation (a) and the combustion geometry assumed for the prechamber spark plug (b).

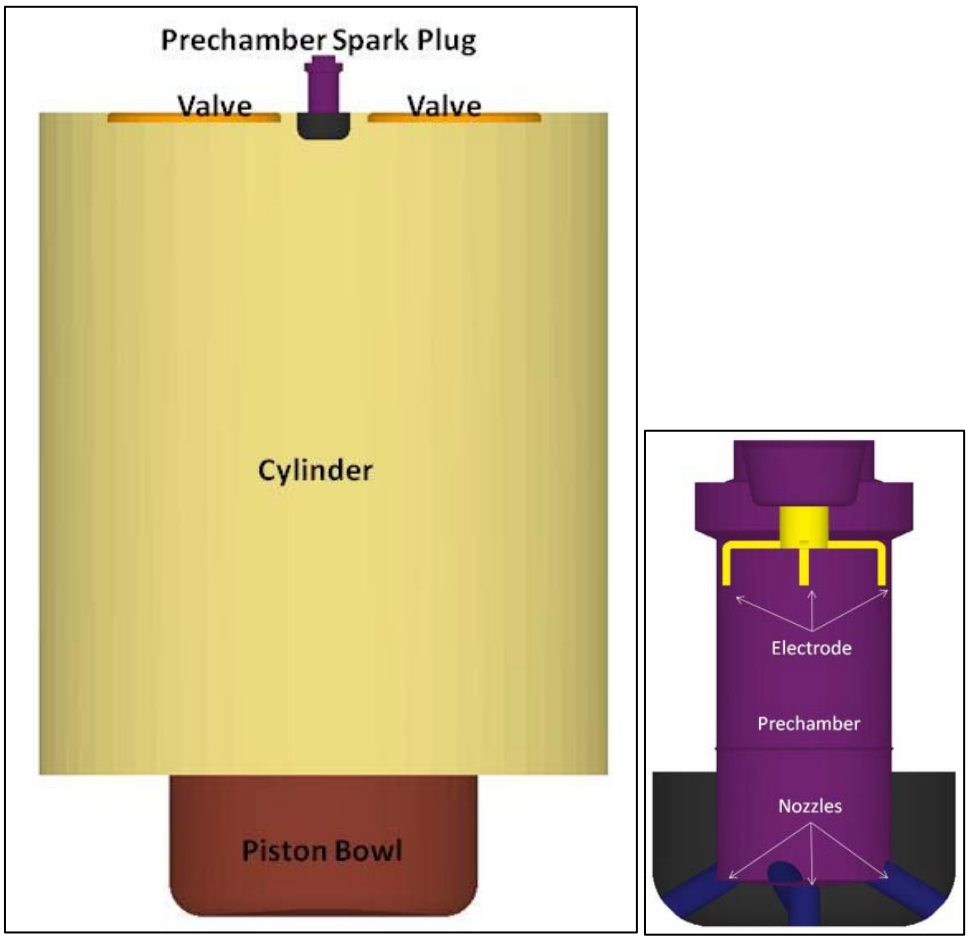

Figure 31. (a) Cross-sectional view of the simulated combustion space; engine and (b) prechamber plug.

A list of some parameters used for the CFD simulation is presented in Table 9.

Table 9. CFD engine simulation parameters.

Engine Cylinder Bore	Motoring Pressure Trace (full speed and load conditions, no ignition)
Engine Piston Stroke	Average Spark Plug Temperatures (at full load)
Connecting Rod Length	Average In-Cylinder Wall Temperatures (combustion side, at full load)
Volumetric Compression Ratio	Spark Timing
Distance between top of piston and head at TDC	Spark Energy Profile
Intake port and valve geometry	Fuel Composition (CH4, C2H6, C3H8, C4H10, CO2, N2, etc)
Exhaust port and valve geometry	Air mass flow rate
Cylinder Head Geometry (Combustion Side)	Fuel mass flow rate
Piston Geometry (Combustion Side)	Air-Fuel Mixture Lambda
Spark Plug Geometry (firing end, including prechamber)	In-Cylinder trapped mass
Intake and Exhaust Valve Lift Profiles	Combustion Pressure Trace (Average of minimum 300 cycles with standard deviation at full load)
Intake Port Temperature	NOx emission level
Intake Port Pressure	Exhaust Port Pressure
Exhaust Port Temperature	Engine Speed

The selected turbulent and heat transferred models were the Reynolds Averaged Navier-Stokes (RANS) with rapid distortion and Renormalization Group (RNG) k-ε [38].and the heat transfer model from Amsden and O'Rourke [40].

The fuel composition, by % volume, measured during engine testing and entered in the simulation was as follows:

$CH_4 \rightarrow 86.63\%$

$C_2H_6 \rightarrow 6.11\%$

$CO_2 \rightarrow 5.85\%$

$N_2 \rightarrow 1.41\%$

Also, shown in Figure 32 is the meshing strategy used in this simulation. It can be seen that very fine mesh were used in the prechamber and at the flame jet location. This approach is necessary to achieve good accuracy of results.

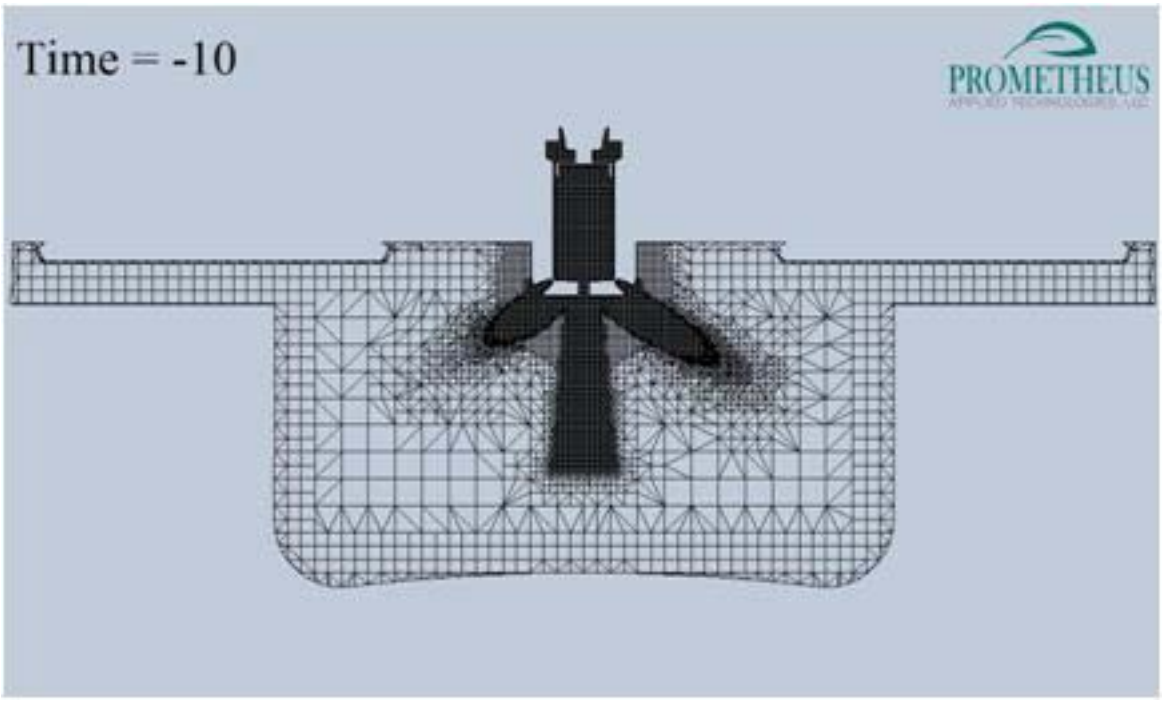

Figure 32. Meshing strategy used in the CFD simulation. Figure obtained from Converge CFD results and visualized trough EnSight visualization software. Note: the mesh shown in this figure is not representative of the actual Converge CFD mesh for the sections were uneven triangles are created. Actual squares are created in the CFD mesh. This is the effect of a visualization setting in the post-processor.

The CFD simulation runs were carried out with the DRM22 mechanism, the MD19

mechanism, and the Nagy21_Burke_MD19 mechanism. The effect of the chemical kinetic mechanism on the simulated in-cylinder combustion process is described in the following CFD flame visualization sequences, represented by isothermal surfaces of 2000 K, compared at specific crank angle positions. Depicted in Figure 33 and Figure 34 is the comparison of the initial flame kernel growth resulting from the two mechanisms. From the size of the flame envelope, one can readily infer that the DRM22 mechanism computes faster combustion rates that the MD19.

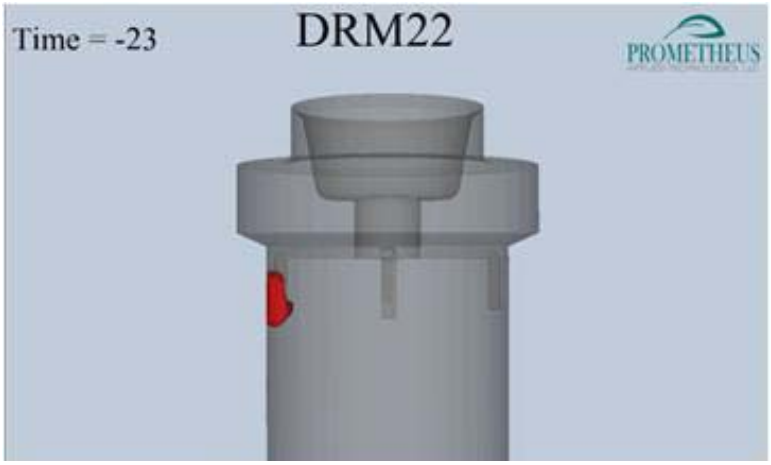

Figure 33. Initial flame development modeled with DRM22. Figure obtained from Converge CFD results and visualized trough EnSight.

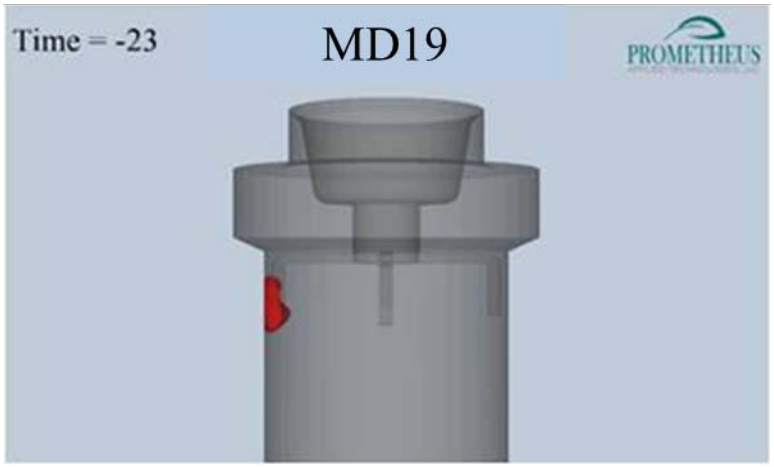

Figure 34. Initial development of flame kernel at one CAD after spark for MD19 mechanism.

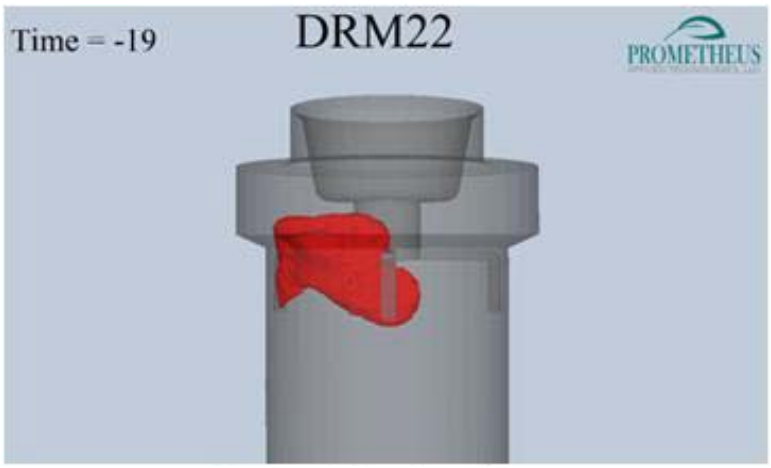

Figure 35. Development of flame kernel at 5 CAD after spark DRM22.

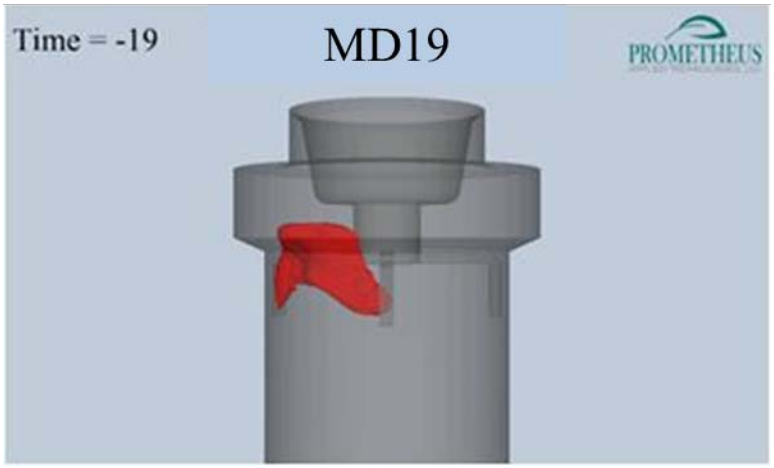

Figure 36. Development of flame kernel at 5 CAD after spark MD19.

The initial flame kernel development is presented in Figures 35 and 36. At this point, the difference in flame size is similar but smaller for the MD19 mechanism.

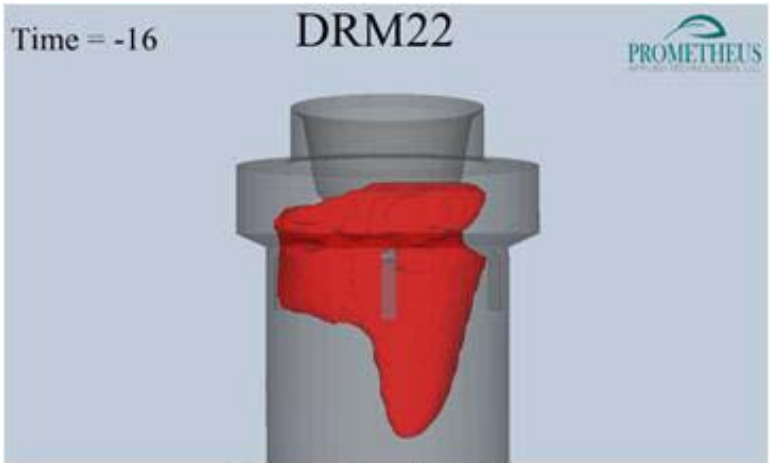

Figure 37. Development of flame kernel at 8 CAD after spark DRM22.

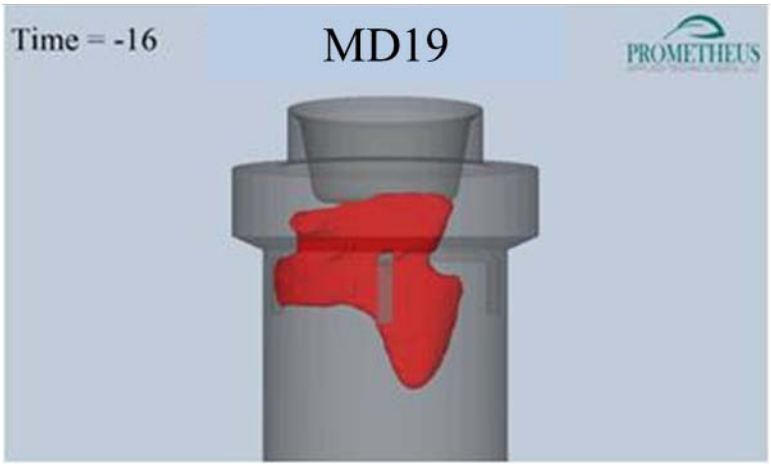

Figure 38. Development of flame kernel at 8 CAD after spark MD19.

The flame kernel growth is shown 8 crank angle degrees after spark in Figures 37 and 38. When the fuel contained in the pre-combustion chamber volume is consumed, flame torches are formed out of the end-cap orifices of the pre-combustion chamber to develop into the main combustion chamber. The difference in flame propagation at -10 CAD before top dead center for the two mechanisms is presented in Figure 39 and Figure 40.

These figures at -10 crank angle degrees clearly indicate that a much more rapid flame jet development is computed with the DRM22 mechanism. In fact, at 8 crank angle degrees before

Top Dead Center (TDC), full flame jets are computed by the DRM22, while with the MD19 mechanism the flame jets are still at their initial stage of formation.

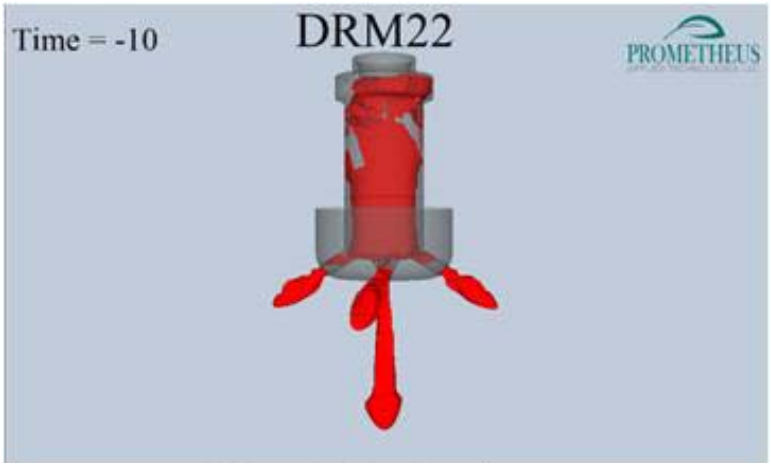

Figure 39. Development of flame torches at 14 CAD after spark DRM22.

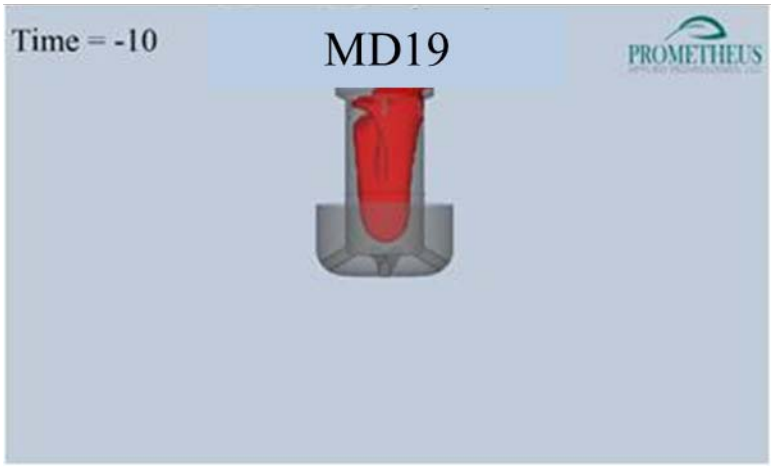

Figure 40. Development of flame torches at 14 CAD after spark MD19.

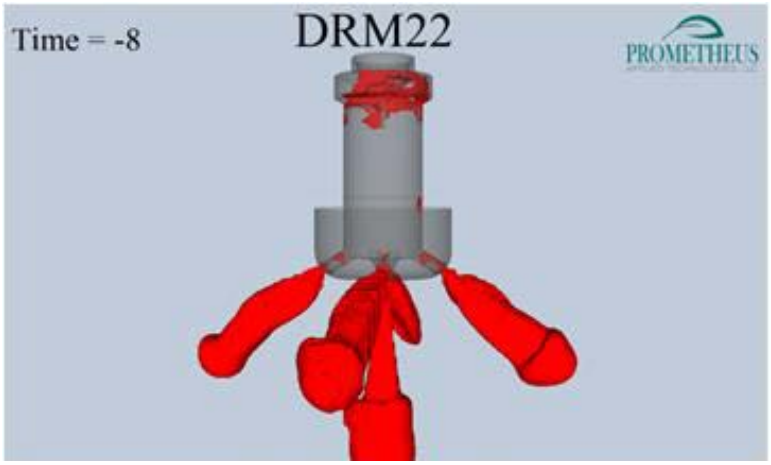

Figure 41. Development of flame torches at 16 CAD after spark DRM22.

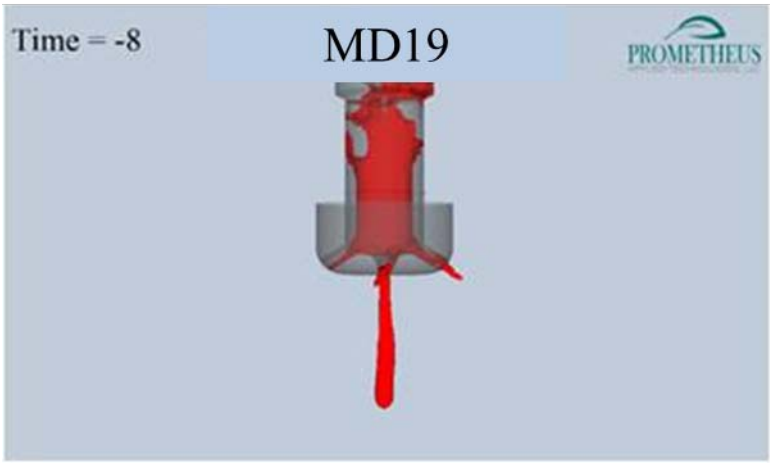

Figure 42. Development of flame torches at 16 CAD after spark MD19.

Figures 41 and 42 show that the combustion run with the DRM22 mechanism has developed complete flame torches out of the pre-combustion chamber, while the MD19 mechanism has only one jet torch formed. Figures 43 and 44 show the flame torches for both mechanisms at -4 crank angle degrees.

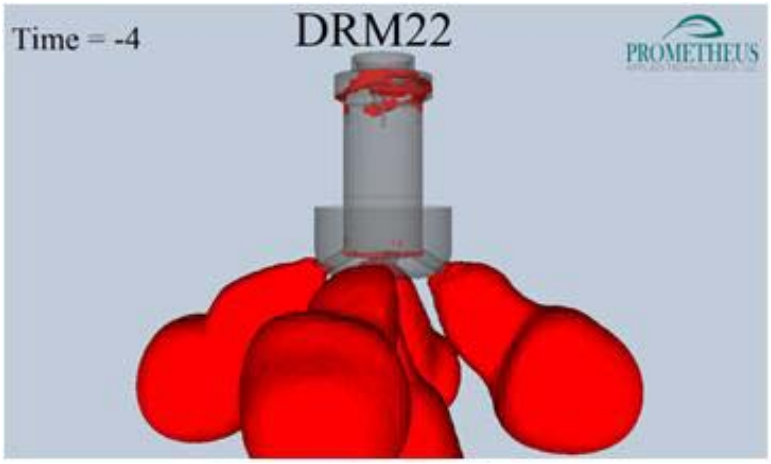

Figure 43. Development of flame torches at 20 CAD after spark DRM22.

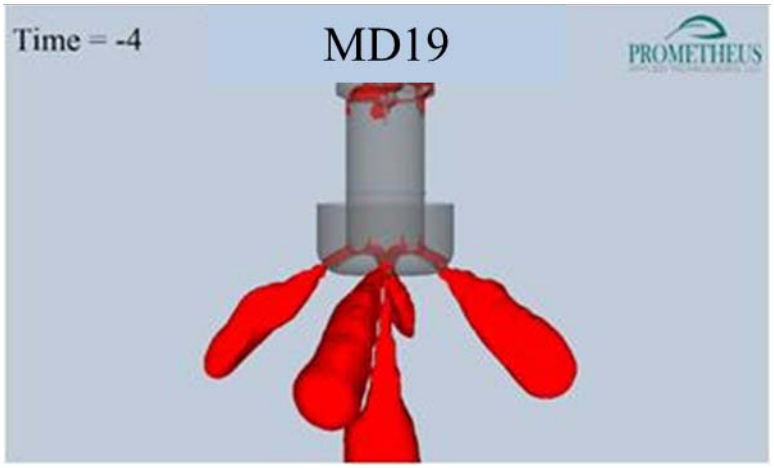

Figure 44. Development of flame torches at 20 CAD after spark MD19.

The sequence from Figure 45 to Figure 50 shows a comparison of the flame front development in the main combustion chamber, from 2 crank angle degrees before TDC to 2 crank angle degrees after TDC. Again, it can be seen that the DRM22 mechanism computes significantly faster flame propagations within the main combustion chamber compared to what is calculated with the MD19 (new mechanism). These results are consistent with the CHEMKIN laminar flame speed calculations previously shown in Table 4.

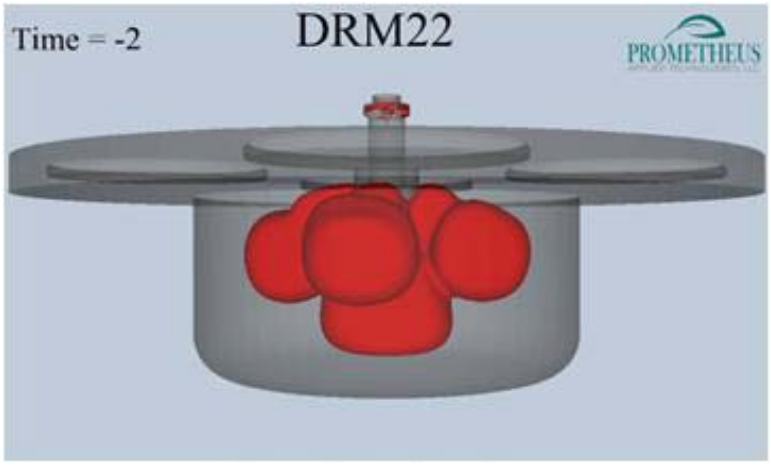

Figure 45. Development of flame front in the main combustion chamber 22 CAD after spark DRM22.

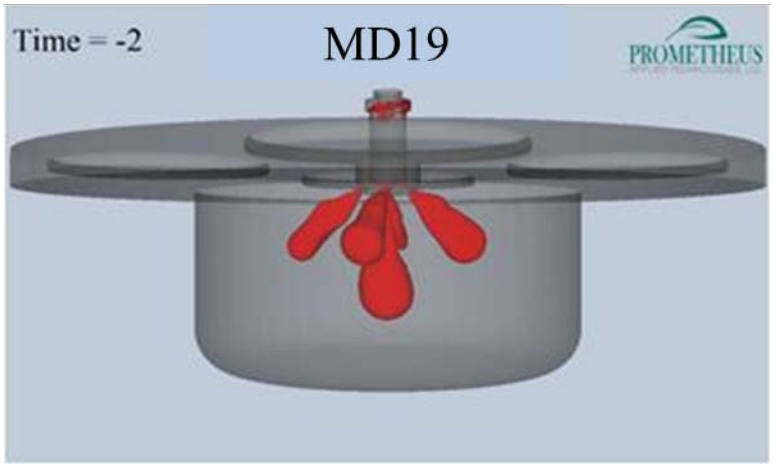

Figure 46. Development of flame front in the main combustion chamber 22 CAD after spark MD19.

Figures 45 and 46 show the flame propagating into the main combustion chamber after the flame torches have reached their maximum penetration length.

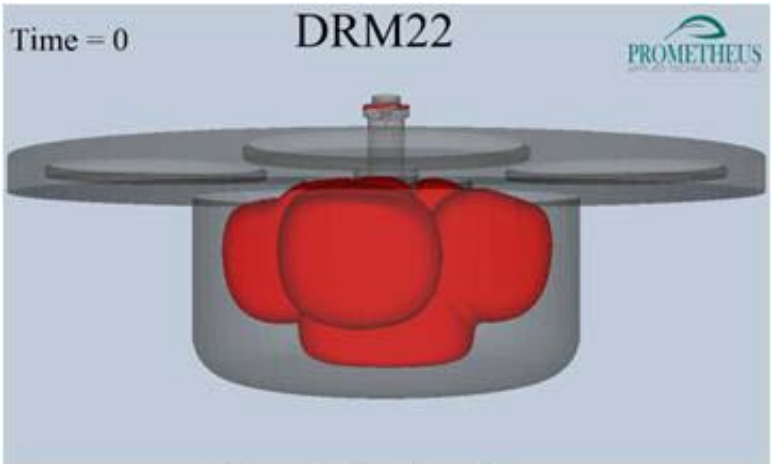

Figure 47. Development of flame front in the main combustion chamber 24 CAD after spark DRM22.

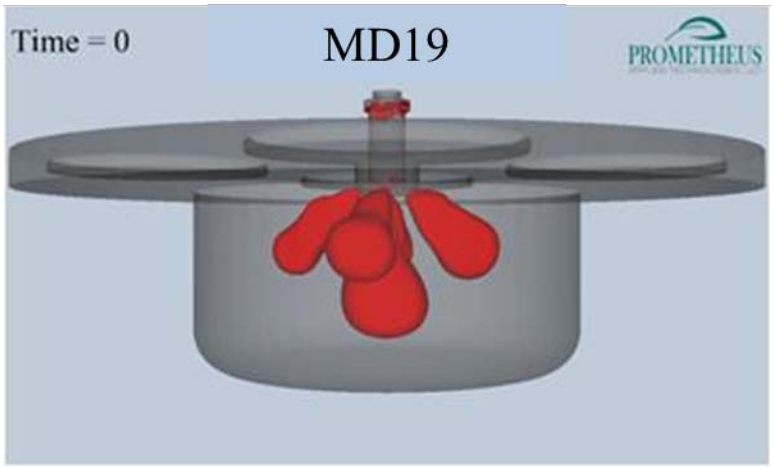

Figure 48. Development of flame front in the main combustion chamber 24 CAD after spark MD19.

Figures 47 and 48 show that while flame front of the DRM22 case has reached the piston bowl, the MD19 combustion has more unburned gas mixture in the main combustion chamber.

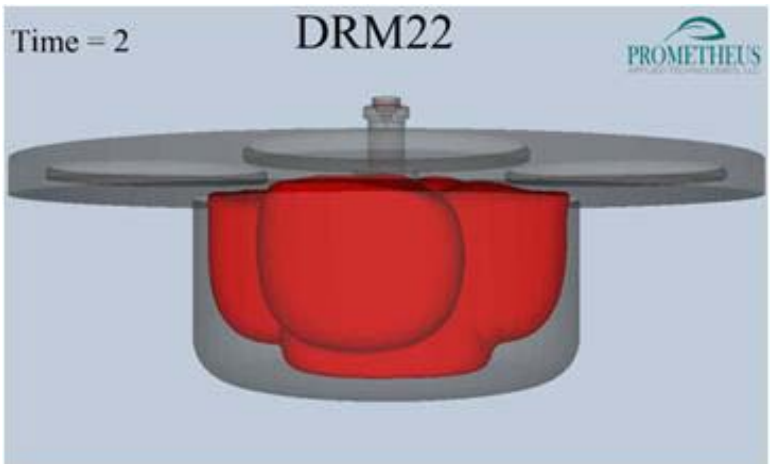

Figure 49. Development of flame front in the main combustion chamber 26 CAD after spark DRM22.

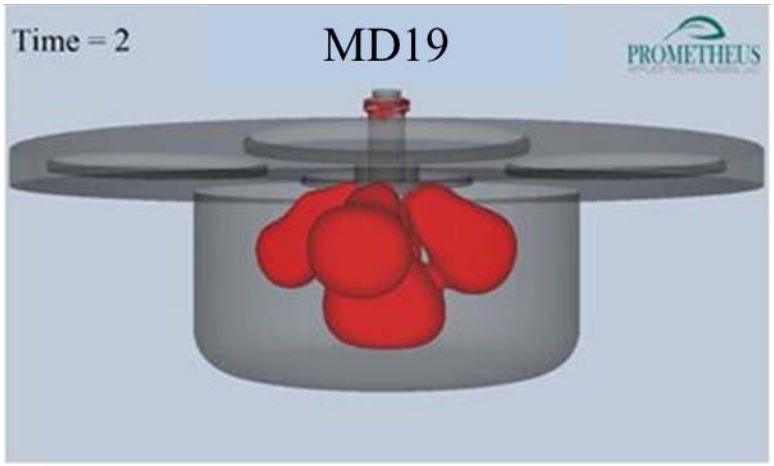

Figure 50. Development of flame front in the main combustion chamber 26 CAD after spark MD19.

The effect observed on flame propagation can also be translated to cylinder combustion pressure rise. Figure 51 shows the results obtained from the CFD simulations for engine cylinder pressure as a function of crank angle. The red line is the result for the DRM22 mechanism. The black dot line is the result for the MD19 mechanism and the black-solid line represents the engine data. It can be seen that the DRM22 significantly over predicts the rate and phasing of combustion, while the MD19 mechanism has much better agreement with the experimental data. The result of the Nagy21-Burke-MD19 mechanism, shown as blue-dashed lines, resulted in

misfire. To obtain a pressure rise, the simulation was re-run with the Nagy21-Burke-MD19 mechanism by increasing the gas temperature by 100 K. This resulted in the orange dash line. To compare to the MD19 at the same conditions, the MD19 was ran at the same initial gas temperature increment of 100 K, resulting in the orange dot line. As the trend shows, the Nagy21-Burke-MD19 computes slower flame speed resulting in a lower pressure curve compared to the MD19 when both simulations had an increase gas temperature of 100 K.

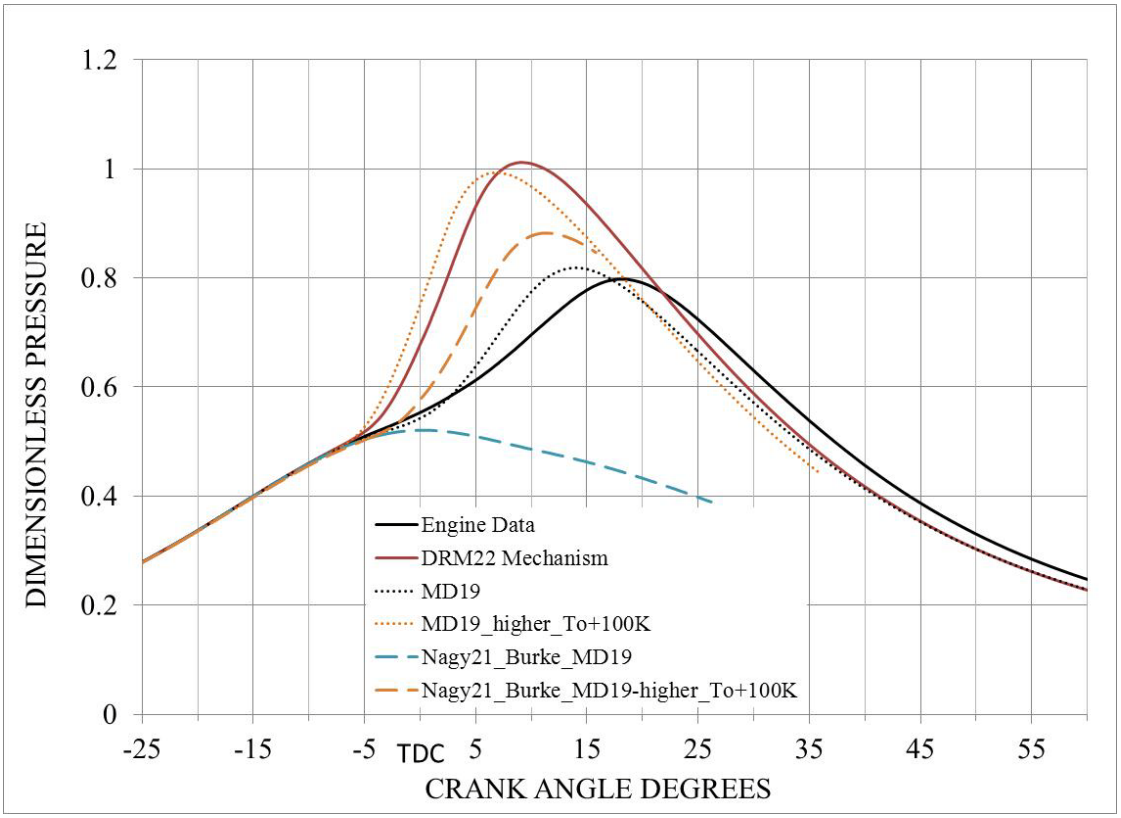

Figure 51. Calculated dimensionless cylinder pressure as a function of crank angle.

The cylinder pressure as a result of the combustion simulation is presented in Figure 51. In terms of rate of combustion, the DRM22 over prediction in flame speed resulted in a faster and higher peak location pressure, while the MD19 and the Nagy21-Burke-MD19 mechanisms have a comparable combustion pressure to that measured on the engine.

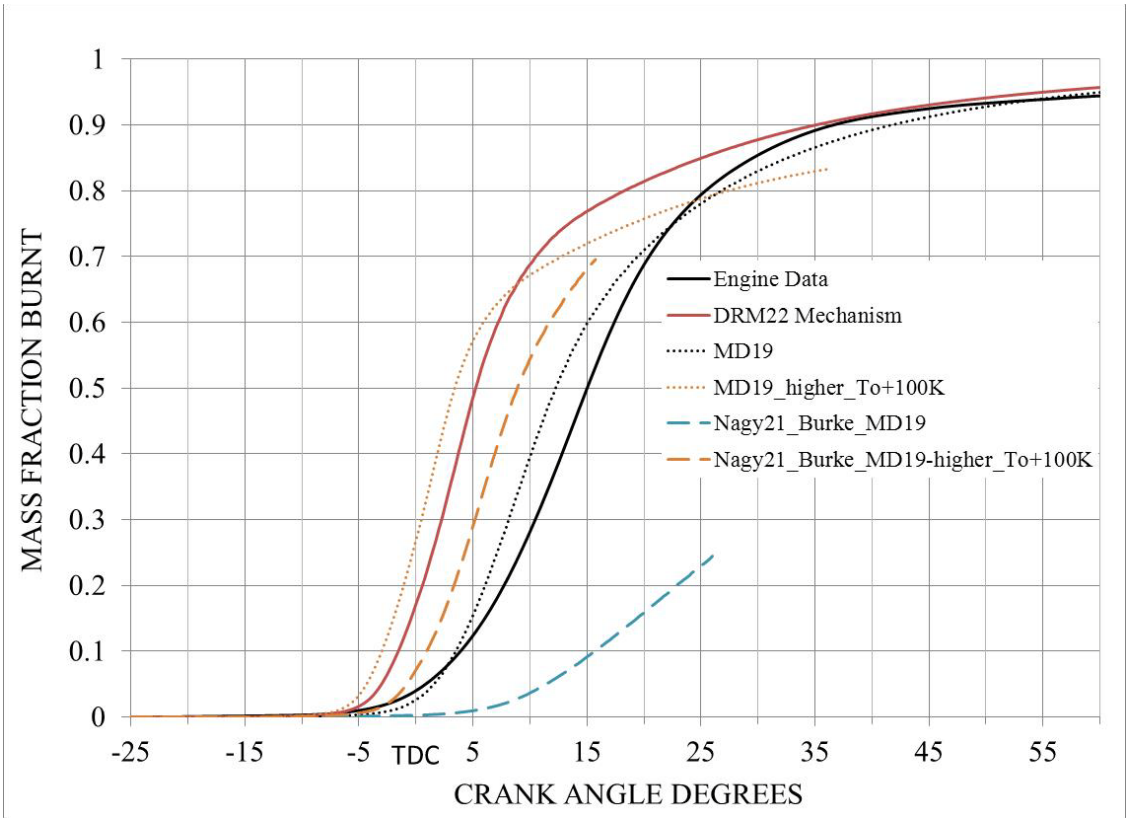

Figure 52. Mass Fraction Burnt (MFB) as a function of crank angle.

The resulting fuel mass fraction burnt as function of crank angle is presented in Figure 52. The DRM22 resulted in the fastest start of combustion at the initial temperature conditions. After adjusting the initial gas temperature by a 100 K increase, the MD19 resulted in faster start of combustion compared to Nagy21-Burke-MD19. It is expected that a similar increase of 100 K with the DRM22 would result in the faster mass fraction burnt curve.

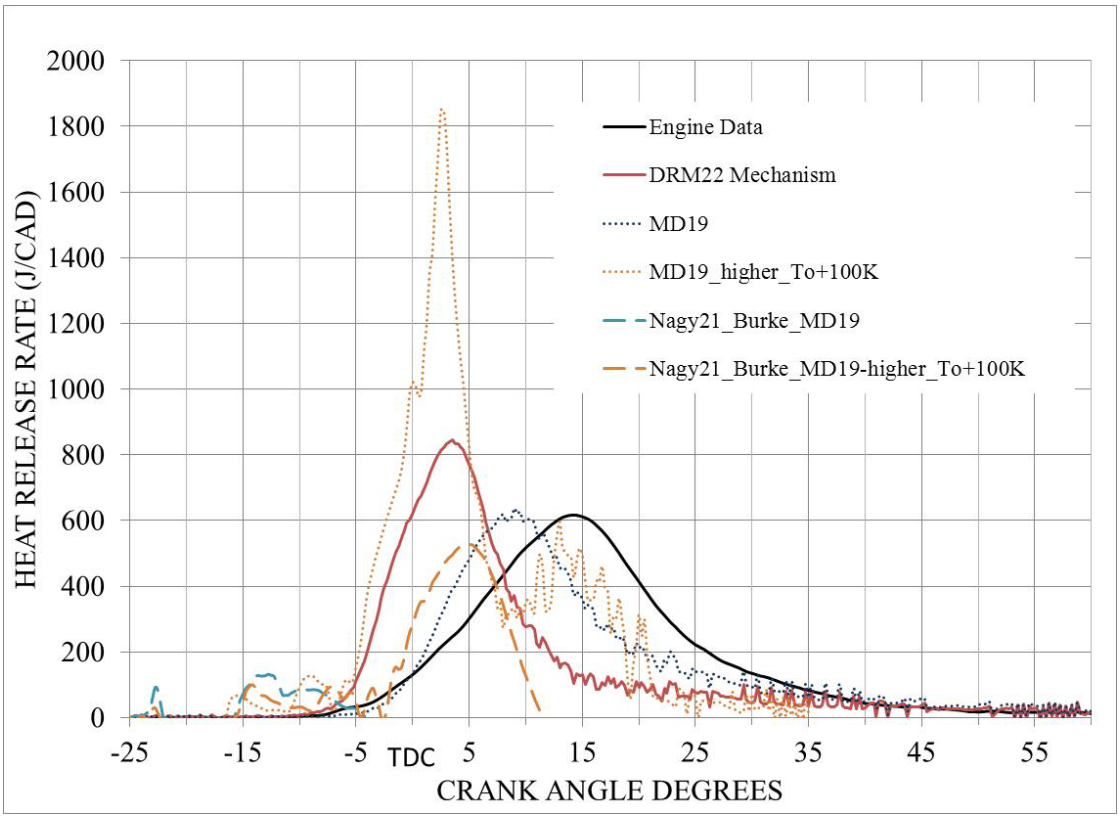

Figure 53. Combustion heat release rate (HRR) as a function of crank angle.

More specifically, Figure 52 and Figure 53 of the MFB and HRR, respectively, show that the predicted start of combustion and combustion duration are between 8 and 10 crank angle degrees more advanced than the experimental data with the DRM22, whereas for the MD19 and the Nagy21-Burke-MD19 mechanisms the difference is within 6 crank angle degree. In terms of rate of combustion, DRM22 over predicts by more than 25%, while the MD19 and the Nagy21-Burke-MD19 mechanisms have a rate of combustion comparable to that measured on the engine. This result is consistent with the reduced laminar flame speed calculated with CHEMKIN, at elevated pressures, for the MD19 mechanism in comparison with DRM22.

In terms of computational time, the MD19 mechanism was approximately 10% faster than the DRM22 at 133 hours versus 147 hours. The difference in computational speed is the result of the reduced number of species and reactions used in the MD19 mechanism. Both

simulations were performed with the same computer having the following specifications: 8 parallel processors at 2.66GHz with 16GB RAM.

6. CONCLUSIONS AND FUTURE WORK

Two new reduced chemical kinetic mechanisms (on the order of 20 species) for methane combustion at high pressures and lean conditions are presented. They compare favorably against measured laminar flame speed data at these conditions and CFD engine simulations using this mechanism reproduce in-cylinder pressure data of high efficiency, lean-burn natural gas engines. The MD19 mechanism is suitable for CFD applications where a reduced number of species and reactions are preferred for computational speed, with an acceptable 29% error in laminar flame speed prediction at 20 atm. The Nagy21-Burke-MD19 mechanism is also suitable for CFD applications, and it is an improvement over the MD19 since it better matches autoignition delay to experimental data. The reaction path analysis showed a similar path for the CH_4 molecule oxidation for the different kinetic mechanisms.

Additional validation and improvement of the reduced mechanisms will be possible by computing laminar flame speed at higher pressures and comparing to experimental data available with different inert gases such as helium and argon that allow for measurements of laminar flame speed at higher pressures without flame disruption. Further enhancement of CFD predictability can also be achieved by using improved sub-models, such as the spark model, the heat transfer model, and the turbulent model. These are the areas where future work will be concentrated.

Another aspect that requires future research is in using the H_2/O_2 sub-mechanisms to affect the reactivity of methane by using hydrogen as a reactant in the fuel instead of higher hydrocarbons such as ethane and propane. The Methane Number definition can be used as a surrogate for the higher alkane content in natural gas and through a comparison based analysis it can be possible to use hydrogen as a surrogate species in a reduced methane mechanisms to simulate the different compositions of natural gas.

Use of CFD for new small engines applications using natural gas with more detailed kinetic mechanisms for combustion may be possible, since the engine size is smaller compared to high BMEP engines, making the computational time more reasonable. Scaling down engine geometry by half provides approximately 300% reduction in computational time, going from a 700mm bore engine to 350mm. An even smaller engine could potentially run with a 50 species mechanism and balance the increase in computational time due to the larger mechanism (estimated increase from 11hrs using a 22 species mechanism, to 15 days for a combustion cycle simulation using a 50 species mechanism in a 350mm bore engine). Further advances are needed to model the effect of larger hydrocarbons, such as propane, in a reduced natural gas mechanism that better predicts the influence of C3 or higher species affecting low temperature chemistry, autoignition phenomena, and flame speed.

REFERENCES

[1] U.S. Department of Energy, "2010 Annual Energy Review," DOE/EIA-0384(2010)

[2] British Petroleum, "Natural Gas Reserves"; http://www.bp.com/sectiongenericarticle800.do?categoryId=9037178&contentId=7068624 (seen on 7/22/2012).

[3] Chevron, "Natural Gas from Shale; Unlocking Energy From Shale Rock Formations"; http://www.chevron.com/deliveringenergy/naturalgas/shalegas/?utm_campaign=Shale&utm_medium=cpc&utm_source=Google&utm_term=Shale_Gas (seen on 7/22/2012)

[4] U.S. Department of Energy, "Transmission, Distribution & Storage", http://fossil.energy.gov/programs/oilgas/delivery/index.html (5/16/12)

[5] Obras Mexico. www.obrasweb.mx/construccion2011/11/08/mexico-invertira-10000-mdd-en-gas-natural (seen on 5/30/12)

[6] Tozzi L., Sotiropoulou E., Harral J., Miller-Lionberg D., and Benson K., "Passive prechamber spark plugs: Then and now", Proceedings of the 7th Dessau Gas Engine Conference (2011) pp. 157-168.

[7] Rozenchan G., Zhu D. L., Law C. K., and Tse S. D., "Outward propagation, burning velocities, and chemical effects of methane flames up to 60 atm," Proc. Combust. Inst., 29, (2002), pp. 1461–1470.

[8] Hunter T.B., Wang H., Litzinger T.A., and Frenklach M., "The oxidation of methane at elevated pressures: Experiments and modeling", Combust. Flame, 97, (1994), pp. 201-224.

[9] Kazakov A., and Frenklach M., Reduced reaction sets based on GRI-Mech1.2, http://www.me.berkeley.edu/drm/ (viewed on 10/20/11).

[10] Smith G.P., Golden D.M., Frenklach M., Moriarty N.W., Eiteneer B., Goldenberg M., Bowman T., Hanson R.K., Song S., Gardiner Jr. W.C., Lissianski V.V., and Qin Z., GRI-Mech, available at http://www.me.berkeley.edu/gri_mech/

[11] Gu X. J., Haq M. Z., Lawes M., and Woolley R., "Laminar burning velocity and Markstein lengths of methane-air mixtures," Combust. Flame, 121, (2000), pp. 41–58.

[12] Curran H.J., Gallagher S.M., and Simmie J.M., "A comprehensive modeling study of methane oxidation," Proceedings of the European Combustion Meeting 2003

[13] Lowry W., de Vries J., Krejci M., Petersen E., Serinyel Z., Metcalfe W., Curran H., and Bourque G., "Laminar flame speed measurements and modeling of pure alkanes and alkane blends blends at elevated pressures" Journal of Eng. For Gas Turbines and Power, ASME 091501, (2011) 133.

[14] Curran H.J., “Detailed chemical kinetic modeling; is there life after GRI-MECH3.0?”, Prepr. Pap.-Am. Chem. Soc., Div. Fuel Chem. 2004, 49 (1), 263

[15] Petersen E.L., Kalitan D.M., Simmons S., Bourque G., Curran H.J., and Simmie J.M., “Methane/propane oxidation at high pressures: Experimental and detailed chemical kinetic modeling” Proceedings of the Combustion Institute 31 (2007) 447-454.

[16] Reaction mechanisms at the Combustion Chemistry Centre, National University of Ireland, Galway. Available from: <http://c3.nuigalway.ie/mechanisms.html> (10/19/2011).

[17] Donato N., Aul C., Petersen E., Zinner H., Curran H., Bourque G., “Ignition and oxidation of 50/50 butane isomer blends”, J. Eng. Gas Turbines Power, 132, 051502.

[18] Healy D., Donato N.S., Aul C.J., Petersen E.L., Zinner C.M, Bourque G., Curran H.J., “n-butane: ignition delay measurements at high pressure and detailed chemical kinetic simulations”, Combustion and Flame, 157, 1526-1539.

[19] Healy D., Donato N.S., Aul C.J., Petersen E.L., Zinner C.M., Bourque G., Curran H.J., “Isobutane ignition delay time measurements at high pressure and detailed chemical kinetic simulations”, Combustion and Flame, 157, 1540-1551.

[20] Healy D., Kopp M.M., Polley N.L., Petersen E.L., Bourque G., Curran H.J., “Methane/n-butane ignition delay measurements at high pressure and detailed chemical kinetic simulations” Energy and Fuels, 24, 1617-1627.

[21] Healy D., Kalitan D.M., Aul C.J., Petersen E.L., Bourque G., Curran H.J., “Oxidation of C1-C5 alkane quintenary natural gas mixtures at high pressures”, Energy and Fuels, 24, 1521-1528.

[22] Zsély I.Gy., Nagy T., Simmie J.M., and Curran H.J., “Reduction of a detailed kinetic model for the ignition of methane/propane mixtures at gas turbine conditions using simulation error minimization methods”, Combustion and Flame 2011, in press.

[23] Wang H., You X., Joshi A.V., Davis S.G., Laskin A., Egolfopoulos F., and Law C.K., “USC Mech version II. High-temperature combustion reaction model of H2/CO/C1-C4 compounds. http://ignis.usc.edu/USC_Mech_II.htm, May 2007.

[24] Konnov AA. Detailed reaction mechanism for small hydrocarbons combustion. Release 0.5. (2007) <http://homepages.vub.ac.be/akonnov/>; (viewed on Oct 21, 2011).

[25] Petrova M.V., and Williams F.A., “A small detailed chemical-kinetic mechanism for hydrocarbon combustion”, Combustion and Flame 144 (2006) 526-544.

[26] Egolfopoulos F.N., “Development of Detailed and Reduced Kinetics Mechanisms for Surrogates of Petroleumg-Derived and Synthetic Jet Fuels” – Final Technical Report

[27] Chen Z., Qin X., Ju Y., Zhao Z., Chaos M., and Dryer F., “High temperature ignition and combustion enhancement by dimethyl ether addition to methane-air mixtures”, Proceedings of the Combustion Institute 31 (2007) 1215-1222.

[28] Zhao Z., Chaos M., Kazakov A., and Dryer F., “Thermal decomposition reaction and a comprehensive kinetic model of dimethyl ether”, International Journal of Chemical Kinetics 40 (2008) 1-18.

[29] Rasmussen C.L., Jakobsen J.G., and Glarborg P., “Experimental measurements and kinetic modeling of CH4/O2 and CH4/C2H6/O2 conversion at high pressure” International Journal of Chemical Kinetics 40 (2008) 778-807.

[30] Huang J., and Bushe W.K., “Experimental and kinetic study of autoignition in methane/ethane/air and methane/propane/air mixtures under engine-relevant conditions”, Combustion and Flame 144 (2006)74-88.

[31] Jomaas G., Zheng X. L., Zhu D. L., and Law C. K., “Experimental determination of counter-flow ignition temperatures and laminar flame speeds of C2-C3 hydrocarbons at atmospheric and elevated pressures,” Proc. Combust. Inst., 30, (2005), pp. 193–200.

[32] Westbrook C. and Dryer F., “Chemical kinetic modeling of hydrocarbon combustion” Progr. Energ. Combust. Sci. 1984, 10, 1-57

[33] Burke M.P., Chaos M., Ju Y., Dryer F.L., Klippenstein S.J., “Comprehensive H2/O2 kinetic model for high-pressure combustion” In Press 2011

[34] Leiker M., Christoph K., Rankl M., Cantellieri W., Pfeifer U., (AVL, Graz, Austria), “Evaluation of anti-knocking property of gaseous fuels by means of methane number and its practical application to gas engines”, ASME-72-DGP-4, 1972.

[35] CHEMKIN Theory Manual, CK-THE-10101-0810-UG-1, Reaction Design 2010

[36] Convergent Science, Inc. http://convergecfd.com/

[37] Senecal P. K., Pomraning E., and Richards K. J., “Multi-Dimensional Modeling of Direct-Injection Diesel Spray Liquid Length and Flame Lift-off Length using CFD and Parallel Detailed Chemistry,” SAE Paper No. 2003-01-1043, 2003.

[38] CONVERGE CFD manual, “CONVERGE^{TM}: A three-dimensional computational fluid dynamics program for transient or steady state flows with complex geometries (version 1.3), March 2008.

[39] Combustion Physics, Chung K. Law, Cambridge University Press, 2006.

[40] Amsden, A. A., O'Rourke, P. J. and Butler, T. D., "KIVA-II: A Computer Program for Chemically Reactive Flows with Sprays," Los Alamos National Laboratory Report No. LA-11560-MS, 1989.